Department of Applied Physics

Ultra-thin insulating layers of hexagonal boron nitride for high-resolution scanning tunneling spectroscopy

Fabian Schulz

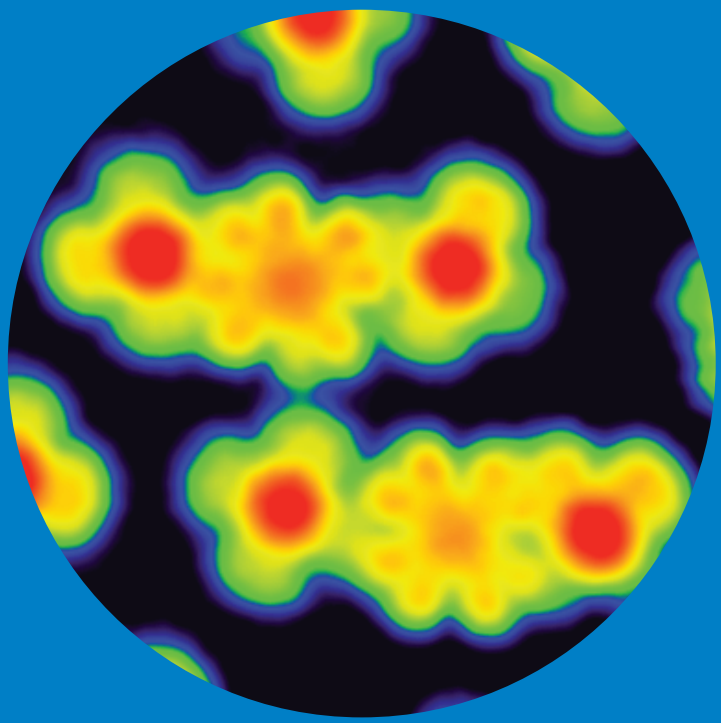

Aalto University

DOCTORAL DISSERTATIONS

Aalto University publication series
DOCTORAL DISSERTATIONS 163/2016

Ultra-thin insulating layers of hexagonal boron nitride for high-resolution scanning tunneling spectroscopy

Fabian Schulz

A doctoral dissertation completed for the degree of Doctor of Science (Technology) to be defended, with the permission of the Aalto University School of Science, at a public examination held at the lecture hall M1 of the school on 16 September 2016 at 12 o'clock.

Aalto University
School of Science
Department of Applied Physics
Atomic Scale Physics

Supervising professor
Professor Dr. Peter Liljeroth

Preliminary examiners
Dr. Ruslan Temirov, Peter Grünberg Institut, Germany
Professor Dr. Ivan Brihuega, Universidad Autónoma de Madrid, Spain

Opponent
Dr. Pavel Jelínek, Institute of Physics of the Czech Academy of Science, Czech Republic

Aalto University publication series
DOCTORAL DISSERTATIONS 163/2016

ISBN 978-952-60-6967-8 (printed)
ISBN 978-952-60-6966-1 (pdf)
ISSN-L 1799-4934
ISSN 1799-4934 (printed)
ISSN 1799-4942 (pdf)
http://urn.fi/URN:ISBN:978-952-60-6966-1

Unigrafia Oy
Helsinki 2016

Finland

441 697
Printed matter

Aalto University

Abstract

Aalto University, P.O. Box 11000, FI-00076 Aalto www.aalto.fi

Author
Fabian Schulz

Name of the doctoral dissertation
Ultra-thin insulating layers of hexagonal boron nitride for high-resolution scanning tunneling spectroscopy

Publisher School of Science

Unit Department of Applied Physics

Series Aalto University publication series DOCTORAL DISSERTATIONS 163/2016

Field of research

Manuscript submitted 15 April 2016 **Date of the defence** 16 September 2016

Permission to publish granted (date) 19 August 2016 **Language** English

☐ **Monograph** ☒ **Article dissertation** ☐ **Essay dissertation**

Abstract

Scanning tunneling spectroscopy (STS) allows for probing the local density of states of surfaces and adsorbates with atomic spatial resolution. When molecules or other nanostructures are electronically decoupled from the surface, STS can be interpreted in terms of the electronic structure of the isolated adsorbate. Ultra-thin insulating layers of metal oxides or alkali halides are commonly used to decouple single molecules and atoms. This thesis explores the possibilities of an alternative decoupling material: hexagonal boron nitride (h-BN).

We start by investigating the atomic-scale structure and electronic properties of an h-BN monolayer on Ir(111) and find that it is characterized by a moiré superstructure with a work function modulation of approx. 0.5 eV. Subsequent STS experiments on molecules deposited onto the h-BN/Ir(111) system indicate their efficient decoupling from the metallic substrate and local charging through the h-BN work function modulation. Comparing molecules in different charge states, we go beyond the prevalent single-particle picture when interpreting STS on molecules and explain the observed resonances as a series of many-body excited states. Finally, we utilize h-BN covalently attached to graphene (G) islands to decouple the G edges from the metallic substrate. This gives rise to an electronic state at the h-BN/G interface, which closely resembles the edge state theoretically predicted for pristine graphene edges.

The work presented in this thesis opens new avenues for high-resolution STS on molecular systems using h-BN as an ultra-thin insulating layer.

Keywords scanning tunneling microscopy, tunneling spectroscopy, self-assembly, single molecules, hexagonal boron nitride, graphene

ISBN (printed) 978-952-60-6967-8 **ISBN (pdf)** 978-952-60-6966-1

ISSN-L 1799-4934 **ISSN (printed)** 1799-4934 **ISSN (pdf)** 1799-4942

Location of publisher Helsinki **Location of printing** Helsinki **Year** 2016

Pages 89 **urn** http://urn.fi/URN:ISBN:978-952-60-6966-1

Preface

The cover of this thesis states that I am its sole author but the truth is, research is always a team effort, so there are plenty of people to thank. First of all, I would like to thank Peter Liljeroth for giving me the opportunity to pursue my PhD in his group, for all his guidance and support and lastly, for not taking all my silly jokes too seriously. Big thanks also to all the other current, past and semi-members of the Atomic Scale Physics group for the fruitful (scientific) discussions, their helping hands and most importantly, the very enjoyable working atmosphere they created. In alphabetical order: Amina, Avijit, Ben, Jani, Kaustuv, Nurul, Päivi, Robert, Sampsa and Shawulienu.

I also would like to thank our collaborators from the dark side, i.e. theory and computational physics, for their insight and patience when sharing it with us: From the Quantum Many-Body Physics group, leader Ari Harju and Andreas, Mari and Mikko, and Ari P. Seitsonen from ENS in Paris, in particular for his attempts to share some of his DFT wisdom with me and his refreshingly critical attitude towards it.

From my previous group at FU Berlin, I would like to thank Christian Lotze for the numerous and lengthy email exchanges that helped me so much to improve the performance of our microscope here at Aalto.

Finally, I would like to thank all my friends and family for their support, in particular Sari Kokkola.

Helsinki, August 19, 2016,

Fabian Schulz

Contents

List of Publications

This thesis consists of an overview and of the following publications which are referred to in the text by their Roman numerals.

I Fabian Schulz, Robert Drost, Sampsa K. Hämäläinen, Thomas Demonchaux, Ari P. Seitsonen and Peter Liljeroth. Epitaxial hexagonal boron nitride on Ir(111): A work function template. *Physical Review B* ***78***, 235429, 2014.

II Fabian Schulz, Robert Drost, Sampsa K. Hämäläinen and Peter Liljeroth. Templated self-assembly and local doping of molecules on epitaxial hexagonal boron nitride. *ACS Nano* ***7***, 11121-11128, 2013.

III Fabian Schulz, Mari Ijäs, Robert Drost, Sampsa K. Hämäläinen, Ari Harju, Ari P. Seitsonen and Peter Liljeroth. Many-body transitions in a single molecule visualized by scanning tunnelling microscopy. *Nature Physics* ***11***, 229-234, 2015.

IV Robert Drost, Andreas Uppstu, Fabian Schulz, Sampsa K. Hämäläinen, Mikko Ervasti, Ari Harju and Peter Liljeroth. Electronic States at the graphene-hexagonal boron nitride zigzag interface. *Nano Letters* ***14***, 5128-5132, 2014.

Author's Contribution

Publication I: "Epitaxial hexagonal boron nitride on Ir(111): A work function template"

The author carried out the majority of the measurements and their analysis and wrote the manuscript.

Publication II: "Templated self-assembly and local doping of molecules on epitaxial hexagonal boron nitride"

The author carried out the measurements and the majority of their analysis and wrote the manuscript.

Publication III: "Many-body transitions in a single molecule visualized by scanning tunnelling microscopy"

The author carried out the measurements and the majority of their analysis and co-wrote the manuscript.

Publication IV: "Electronic States at the graphene-hexagonal boron nitride zigzag interface"

The author carried out a part of the measurements and took part in discussing and analyzing the data.

1. Introduction

Scanning tunneling spectroscopy (STS) combines atomic spatial resolution with current-voltage spectroscopy, enabling measurements of the electronic structure of single molecules and atoms [1–6]. Such experiments are of paramount importance for the understanding of fundamental aspects of charge and spin transport, as well as related phenomena. Offering a well-controlled environment, they minimize the complexity of the investigated system down to its quintessential components, instead of suffering from ensemble averages or external perturbations.

STS draws upon the scanning tunneling microscope (STM) [7], a tool which measures the quantum mechanical tunneling current between a conducting sample and a very fine probe to generate a topographic image of the sample surface. The tunneling current depends on the overlap between the tip and sample wave functions and when measured as a function of applied voltage, allows deducing the local density of states (LDOS) of the sample. Generally, this quantity will reflect the properties of the combined system of substrate and possible adsorbates and depending on the interaction strength, the adsorbate's electronic structure may be altered by the surface. For single atoms or molecules, the gas-phase electronic structure consists of discrete, δ-function-like energy levels. If the surface-adsorbate interaction upon adsorption is weak, this picture does not change significantly except that (i) the observed levels broaden into a Lorentzian due their finite life time as they couple to states of the substrate [8–10] and (ii) the fundamental gap is reduced due to screening effects [10]. The magnitude of the broadening depends on the coupling between adsorbate and substrate states and can be on the order of 0.1 meV to 1 eV [11]. If the interaction is very strong, hybridization can result in mixed adsorbate-surface electronic states which neither resemble the unperturbed substrate or adsorbate wave functions [10].

It is thus clear that STM/STS studies focusing on the electronic properties of single molecules or atoms require means to minimize hybridization with the substrate electronic states. As STM demands conducting samples, using bulk insulators as a substrate is not an option. This limitation can be overcome by growing ultra-thin insulating layers on metallic substrates [12] (Fig. 1.1). Usually around two to three atoms thick, such layers provide the required electronic decoupling while still allowing a measurable tunneling current to flow.

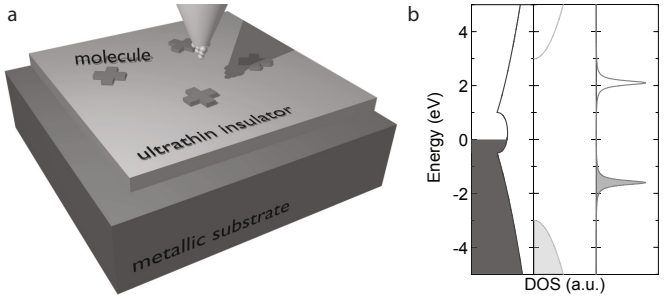

Figure 1.1. (a) Schematic representation of an ultra-thin insulating layer decoupling molecules from a metallic substrate. (b) Idealized DOS of the different materials, from left to right: metal (two parabolic bands crossing around the Fermi level), insulator (two parabolic bands separated by an energy gap), molecule (two life-time broadened Lorentzians). Zero energy denotes the Fermi level; states below this energy are occupied (dark shaded) and above it unoccupied.

The use of decoupling thin films in STM has facilitated significant progress in the investigation of isolated adsorbate properties, such as imaging of individual molecular orbitals [13], single-atom spin-flip spectroscopy [14], manipulation and control over the charge states of atoms [15, 16] and molecules [17, 18] or different aspects of electron-vibration coupling [19–21]. The two most commonly employed families of ultra-thin insulators are metal oxides such as MgO [15, 22, 23] or Al_2O_3 [19, 24, 25] and alkali halides such as NaCl [16, 18, 26] or RbI [20]. Unfortunately, the limit of life time-broadened molecular resonances with Lorentzian shape and peak widths in the meV range is usually not reached on such surfaces [13, 19, 25, 27]. Due to the polar nature of oxides and salts, there is strong electron-phonon coupling between adsorbate states and optical phonons of the insulator's ionic lattice [27], leading to broad, Gaussian line shapes.

A less ionic alternative could be hexagonal boron nitride (h-BN), a wide band-gap insulator [28] isostructural to graphene (G) but composed of alternately arranged boron and nitrogen atoms. While not purely covalently bonded as its carbon counterpart, electronic structure calculations

indicate significant accumulation of charge density in between boron and nitrogen atoms [29, 30], suggesting that the bonding is not purely ionic either. Research in monolayers of h-BN grown on metal substrates [31–34] started to increase roughly one decade ago, when the rise of graphene [35] sparked interest also in other two-dimensional materials. However, the use of h-BN as an ultra-thin insulator for STS has been scarce until a few years ago, with initial contributions focusing on superconducting nanoparticles [36] and molecular magnets [37].

This thesis aims to further explore the potential of h-BN by characterizing its structure when grown on Ir(111) and subsequently investigating its capabilities to decouple different kinds of electronic states. In addition to STS experiments on single molecules adsorbed on top of h-BN, it is shown that graphene edges can also be decoupled from a metallic substrate by covalently attaching h-BN, proving the versatility of the material. The remainder of the thesis is structured as follows: in *Experimental Methods*, the principles of STM and STS are explained, as well as the growth of h-BN and graphene by chemical vapour deposition and the experimental set-up. The *Results* section briefly summarizes the main outcomes of the publications upon which this thesis is based, while *Outlook and Summary* attempts to put the results into a broader perspective. Finally, all the original publications can be found at the end of this document.

2. Experimental methods

2.1 Scanning tunneling microscopy

It is an elementary result of quantum mechanics that the wave function ψ of an electron is not identically zero even within a potential barrier, which is a forbidden region in classical mechanics. Instead, when penetrating the barrier on one side, ψ decays exponentially within the barrier, resulting in a finite probability for the electron to be found at the opposing side (as long as the barrier width z is finite). This is the so-called tunneling effect of quantum mechanics, a sketch of which is shown in Fig. 2.1. In a non-equilibrium situation where the tunneling rates for wave functions impinging on either side of the barrier are different, it can give rise to an appreciable current.

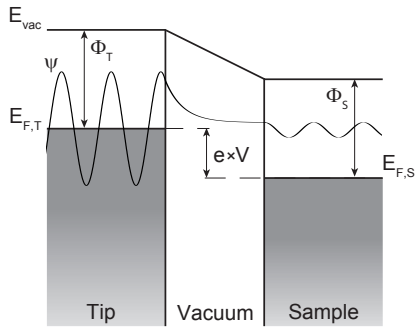

Figure 2.1. Schematic of a tunneling junction with an applied bias voltage V. The wave function ψ is free electron-like in the metallic tip and sample but decays exponentially within the barrier.

This is the underlying principle of the scanning tunneling microscope (STM) [7], a tool which has revolutionized surface science and whose inventors Gerd Binnig and Heinrich Rohrer were awarded the Nobel Prize

in Physics in 1986.[1] The basic idea of the STM is to bring a metallic tip into close proximity of a conducting surface, typically to within 5-10 Ångströms (Å), such that electrons can tunnel from the tip to the surface and *vice versa*. A bias voltage is applied to misalign their Fermi levels and thus, a tunneling current will flow between them. This current will be in the order of pico- or nanoamperes, which can be measured easily and with high precision. While scanning the tip over the surface, the spatial variation of the current is either recorded directly or used as feedback signal to acquire a constant-height or constant-current image of the surface, respectively. The two imaging modes are schematically depicted in Fig. 2.2.

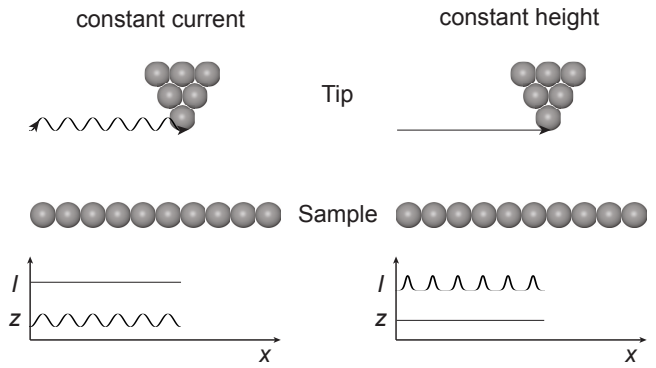

Figure 2.2. (a) Constant-current and (b) constant-height imaging mode.

In the simple approximation of a metal-vacuum-metal tunneling junction, and assuming the work functions ϕ of tip and sample are equal, the current I across the barrier is given by the transmission probability T, which is proportional to the ratio of the amplitudes (given by the absolute square) between the outgoing ψ_z and incoming ψ_0 wave functions:

$$I \propto \frac{|\psi_z|^2}{|\psi_0|^2} \propto e^{-2\kappa z} \quad \text{with} \quad \kappa = \sqrt{2m\phi/\hbar} \quad , \tag{2.1}$$

where $\hbar$ is Planck's constant divided by 2π and m the mass of the electron. For typical values of metallic work functions of around five electronvolts (eV), the current will decrease by one order of magnitude if the tip-sample distance is increased by 1 Å. As a consequence, if one atom of the tip apex is protruding just a bit more towards the sample than all others, the overwhelming majority of the tunneling current will flow between that atom and the surface. This high sensitivity of the current to the tip-sample

[1] Shared with Ernst Ruska for his work on electron optics and design of the first electron microscope.

distance allows STM to image surfaces with atomic resolution [38]. Since STM is best suited for the study of atomically clean surfaces and well-defined nanostructures, experiment are usually carried out in ultra-high vacuum (UHV) to minimize sample contamination. To maximize resolution, the microscope can be operated at low temperatures, which stabilizes the tip-sample junction and reduces drift as well as thermally excited charge carriers.

2.1.1 Bardeen formalism and Tersoff-Hamann approximation

To properly understand the STM image contrast and its origin, a more detailed theory than presented above is needed. Such a theory inevitably has to start with a thorough description of the tunneling process.

In 1961, J. Bardeen worked out a formalism that described tunneling from a many-particle point of view [39]. His approach is basically of perturbative nature, but its beauty arises from simply treating two subspaces with orthogonal sets of wave functions, where the perturbation is the interaction of the two subspaces [40]. He considered a system as shown in Fig. 2.3, with two metals a and b separated by a barrier region $z_a < z < z_b$ and two many-particle wave functions Ψ_0 and Ψ_{mn}, which differ by the transfer of one electron from state m in metal a into state n in metal b. States m and n are described by quasi-particle wave functions ψ_m in a and ψ_n in b, respectively, which both decay exponentially within the barrier region. Thus, Ψ_0 is a solution to the stationary Schrödinger equation with energy E_0 for the subspace $z < z_b$ and Ψ_{mn} is a solution for $z > z_a$ with energy E_{mn}. Even though both are good solutions within the barrier, neither one of them is a good solution for the combined system.

A time-dependent wave function can be constructed by a linear combination of the stationary Ψ_0 and Ψ_{mn}

$$\Psi = a(t)\Psi_0 e^{-iE_0 t/\hbar} + \sum_{mn} b_{mn}(t)\Psi_{mn} e^{-iE_{mn}t/\hbar} \quad , \tag{2.2}$$

which is a solution to the Schrödinger equation with the Hamiltonian H of the combined system

$$i\hbar\partial_t \Psi = H\Psi \quad . \tag{2.3}$$

The coefficient $a(t)$ will remain in the order of unity for weak coupling and small t. Thus, insertion of Eq. 2.2 into Eq. 2.3 and elimination of the sum by forming the inner product with $\Psi^*_{mn'} e^{iE_{mn'}h/t}$ yields the time evolution

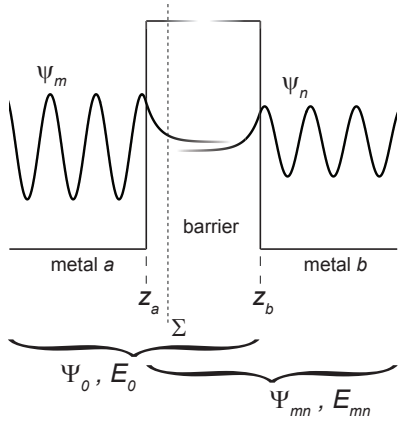

Figure 2.3. Bardeen's model system: Two regions a and b separated by a barrier region $z_a < z < z_b$. The quasi-particle wave functions ψ_m and ψ_n decay exponentially within the barrier. Thus, the many-particle wave functions Ψ_0 and Ψ_{mn} are good solutions in their subsystems and in the barrier, but not for the combined system. Σ is an arbitrary surface within the barrier separating the two subsystems (see text).

for the coefficient b_{mn} to first order:

$$i\hbar\dot{b}_{mn}(t) = \int \Psi^*_{mn}(H - E_0)\Psi_0 \,\mathrm{d}\mathbf{r}\, e^{-i(E_0 - E_{mn})t/\hbar} \quad . \tag{2.4}$$

The derivative $\dot{b}_{mn}$ is related to the transition rate of the electron from state m into state n, allowing for definition of the tunneling matrix element

$$M_{mn} = \int \Psi^*_{mn}(H - E_0)\Psi_0 \,\mathrm{d}\mathbf{r} \quad . \tag{2.5}$$

By construction, the integral in Eq. 2.5 is non-zero only in the subspace $z > z_b$. The expression can be cast into a symmetric form by subtracting $\Psi_0(H - E_{mn})\Psi^*_{mn}$, which is non-zero only for $z < z_a$. After invoking energy conservation, *i.e.* $E_0 = E_{mn}$, the only terms that remain are the ones including the kinetic energy operator:

$$M_{mn} = -\frac{\hbar^2}{2m}\int_b \left(\Psi^*_{mn}\nabla^2\Psi_0 - \Psi_0\nabla^2\Psi^*_{mn}\right)\mathrm{d}\mathbf{r} \quad . \tag{2.6}$$

The subscript b indicates that the integral has to be carried out only for $z > z_b$. Using Green's theorem, it can be transformed into a surface integral

$$M_{mn} = \frac{\hbar^2}{2m}\int_\Sigma \left(\Psi_{mn}\nabla\Psi^*_0 - \Psi^*_0\nabla\Psi_{mn}\right)\mathrm{d}\mathbf{S} \quad , \tag{2.7}$$

where the surface Σ can be any surface lying within the barrier, separating the two subspaces a and b. An expression equivalent to Eq. 2.7 can be derived when considering separate tip and sample wave functions [40].

The tunneling current can be expressed by first-order perturbation theory in terms of the matrix element Eq. 2.7, giving in the limit of small bias voltage V and low temperature [41]

$$I = \frac{2\pi \mathrm{e}^2}{\hbar} V \sum_{mn} |M_{mn}|^2 \delta(E_0 - E_F)\delta(E_{mn} - E_F) \quad , \tag{2.8}$$

where e is the charge of an electron and E_F the Fermi level. Evaluation of the matrix element M_{mn} is the crucial part, which was carried out by J. Tersoff and D. R. Hamann [41, 42] to provide a quantitative theory for STM. The surface wave function ψ_n is expressed in a very general form as a sum over Bloch waves in the plane of the surface, decaying exponentially into the vacuum:

$$\psi_n \propto \sum_G a_G e^{-(\kappa^2 + |\mathbf{k}_{||} + \mathbf{G}|^2)^{1/2} z} e^{i(\mathbf{k}_{||} + \mathbf{G})\mathbf{r}_{||}} \quad , \tag{2.9}$$

where κ is the decay constant as defined in Eq. 2.1 and $\mathbf{k}_{||}$ and $\mathbf{G}$ are the surface wave vector and reciprocal lattice vector, respectively. The difficulty arises from the unknown wave function of the tip ψ_m, and it was the achievement of Tersoff and Hamann to approximate the tip apex as a locally spherical potential well while neglecting its detailed atomic structure. In the gap region, the tip wave function thus exhibits an asymptotic spherical form around the center of curvature of the tip $\mathbf{r}_0$

$$\psi_m \propto \frac{e^{-\kappa|\mathbf{r} - \mathbf{r}_0|}}{|\mathbf{r} - \mathbf{r}_0|} \quad . \tag{2.10}$$

The right-hand side in 2.10 can be expanded in a way analogous to Eq. 2.9 by noting that

$$\frac{e^{-\kappa r}}{r} = \int \frac{e^{-(\kappa^2 + q^2)^{1/2}|z|} e^{i\mathbf{q}\mathbf{r}_{||}}}{2\pi(\kappa^2 + q^2)^{1/2}} \mathrm{d}\mathbf{q} \quad . \tag{2.11}$$

Plugging the surface wave function Eq. 2.9 and the tip wave function Eqs. 2.10 and 2.11 into Eq. 2.7, one finds that the tunneling matrix element is simply proportional to the surface wave function

$$M_{mn} \propto \psi_n(\mathbf{r}_0) \tag{2.12}$$

yielding for the tunneling current via Eq. 2.8

$$I \propto \mathrm{e}^2 V \rho_t(E_F) \sum_n |\psi_n(\mathbf{r}_0)|^2 \delta(E_n - E_F) \quad . \tag{2.13}$$

Here, $\rho_t(E_F)$ is the tip density of states and $\sum_n |\psi_n(\mathbf{r}_0)|^2 \delta(E_n - E_F)$ defines the local density of states (LDOS) $\rho_s(\mathbf{r}_0, E_F)$ of the sample surface at the Fermi level at the center of curvature of the tip. Thus, in the constant

current mode at small bias, the tip follows a contour of constant LDOS. Since the asymptotically spherical tip wave function Eq. 2.10 behaves analogous to real s orbitals computed from spherical modified Bessel functions, this model is also known as s-wave model.

2.1.2 Scanning tunneling spectroscopy

From the preceding section it is clear that when the bias voltage is in resonance with an electronic state of the sample, the tunneling probability and thus the conductance is enhanced. This is reflected in an increased slope of the I-V curve and consequently, peaks in the differential conductance $\mathrm{d}I/\mathrm{d}V$. More precisely, the current for finite bias voltage and temperature is the convolution of the tip and surface DOS integrated over energy [40]:

$$I = \frac{4\pi\mathrm{e}}{\hbar}\int_{-\infty}^{\infty}\left[f(E_F-\mathrm{e}V+\epsilon)-f(E_F+\epsilon)\right]\rho_s(E_F-\mathrm{e}V+\epsilon)\rho_t(E_F+\epsilon)|M|^2\mathrm{d}\epsilon \quad , \tag{2.14}$$

where $f(E)$ is the Fermi distribution function. For low temperatures, $f(E)$ can be approximated by a step function. To first order, the energy dependence of M is given by $M_0 e^{\kappa z\epsilon/\phi}$, yielding for the tunneling current

$$I \propto \int_{-\frac{1}{2}\mathrm{e}V}^{\frac{1}{2}\mathrm{e}V}\rho_s(E_F+\frac{1}{2}\mathrm{e}V+\epsilon)\rho_t(E_F-\frac{1}{2}\mathrm{e}V+\epsilon)e^{\kappa z\epsilon/\phi}\mathrm{d}\epsilon \quad . \tag{2.15}$$

The weighting factor $e^{\kappa z\epsilon/\phi}$ corrects for the fact that states at higher energy have a larger tunneling probability than lower lying ones (higher lying states are closer to the vacuum level and thus have a lower energy barrier). For a typical bias voltage of 1 V ($\epsilon = \pm 0.5$ eV), work function (barrier height) ϕ of around 5 eV and tip-sample distance (barrier width) z of 10 Å, the ratio of the weighting factors at the two limits of the integral is close to 10:1. Thus, at positive sample bias when electrons tunnel from occupied states of the tip into unoccupied states of the sample, contributions from the upper limit of the integral dominate and the differential conductance is proportional to the sample DOS at voltage V:

$$\left.\frac{\mathrm{d}I}{\mathrm{d}V}\right|_{V>0} \propto \rho_s(E_F+\mathrm{e}V)\rho_t(E_F) \quad . \tag{2.16}$$

Conversely, at negative sample voltage when the electrons tunnel from the surface to the tip, the $\mathrm{d}I/\mathrm{d}V$ will be proportional to the tip DOS at voltage V. Only if the tip is prepared such that its DOS is approximately flat, the $\mathrm{d}I/\mathrm{d}V$ signal can also at negative bias voltages be interpreted in terms of the sample DOS.

The capability of STM to probe the (L)DOS with atomic resolution is the driving force underlying the sub-discipline of scanning tunneling spectroscopy. Experimentally, the easiest way to measure the differential conductance is by the use of a lock-in amplifier. The dc bias voltage V is modulated by a small, high-frequency sinusoidal ac component $V_{ac}\sin\omega t$. The resulting modulation of the current is sensitive to the slope of the I-V curve, as can be seen from a Taylor expansion of the current for small modulation voltages:

$$I(V + V_{ac}\sin\omega t) \simeq I(V) + \frac{\mathrm{d}I}{\mathrm{d}V}V_{ac}\sin\omega t + \frac{\mathrm{d}^2I}{\mathrm{d}V^2}V_{ac}^2\sin^2\omega t + \ldots \quad . \tag{2.17}$$

The lock-in amplifier then multiplies the signal of the modulated current by a reference signal of the same frequency ω. Since the integral over time t for the product of two sine functions is non-zero only if their frequencies are equal

$$\lim_{t\to\infty}\frac{1}{t}\int_0^t \sin\omega_1 t' \sin\omega_2 t'\,\mathrm{d}t' = \begin{cases} 1/2 & \text{if } \omega_1 = \omega_2 \\ 0 & \text{otherwise} \end{cases} \quad , \tag{2.18}$$

only the spectral component proportional to the $\mathrm{d}I/\mathrm{d}V$ survives, while all the other components are filtered out. Equation 2.17 shows that also higher derivatives $\mathrm{d}^nI/\mathrm{d}V^n$ are accessible by choosing a reference signal whose frequency is the n-th harmonic of ω.

2.1.3 Interpretation of tunneling spectra

STS does not just allow to measure the DOS of clean surfaces but also of adsorbates, *e.g.* deliberately evaporated single molecules. Unlike the dispersive energy bands found in bulk solid-state systems, in such zero-dimensional objects the DOS is primarily composed of discrete electronic levels. In gas phase, those levels correspond to δ-functions well-separated in energy space. Adsorption on a surface changes this picture, as the levels broaden due to life time effects and hybridization with substrate electronic states. STS on such samples usually will reveal a series of peaks in the $\mathrm{d}I/\mathrm{d}V$ signal which correspond to removal or injection of an electron from or into the combined molecule-surface system. According to Bardeen, the tunneling probabilities are governed by the full many-electron wave functions of tip and sample, which would be impossible to derive for such complex and large systems. Fortunately, we have seen above that under certain circumstances the $\mathrm{d}I/\mathrm{d}V$ signal can be interpreted simply in terms of the sample electronic structure. If further the interaction be-

tween adsorbate and surface can be minimized by an ultra-thin insulating layer [13, 19, 21], tip and substrate can be simply viewed as electron baths and the peaks in STS attributed to different many-electron wave functions of the isolated molecule.

From a theoretical point of view, STS probes transitions between an N-electron wave function Ψ^N and some ($N\pm1$)-electron wave functions $\Psi^{(N\pm1)}$. The response is then given by the diagonal elements of the many-body spectral function [43], i.e.

$$A(\nu,\omega) = 2\pi \sum_k |\langle \Psi_k^{N+1}|c_\nu^\dagger|\Psi_0^N\rangle|^2 \delta(\omega - E_k^{N+1} + E_0^N) \tag{2.19}$$

for injection of an electron at positive sample bias voltage and

$$A(\nu,\omega) = 2\pi \sum_k |\langle \Psi_k^{N-1}|c_\nu|\Psi_0^N\rangle|^2 \delta(\omega - E_k^{N-1} + E_0^N) \tag{2.20}$$

for removal of an electron at negative bias. The matrix element includes the initial state, safely assumed to be the ground state Ψ_0^N at low temperatures, and the possible final states $\Psi_k^{N\pm1}$, the lowest transition being into the ($N\pm1$)-electron ground state denoted by $k = 0$ and subsequent transitions corresponding to excited states $k = 1, 2, 3, \ldots$. [2] $c_\nu^\dagger$ and c_ν are the creation and annihilation operators for an electron in the single-particle orbital ν and the δ-function assures energy conservation.

However, even for few-electron systems within the Born-Oppenheimer approximation, calculation of the exact many-electron wave function is impossible due to the electron-electron interaction term in the many-body Schrödinger equation, which couples all the electrons. Several approximation schemes for *ab initio* electronic structure calculation exist. The Hartree-Fock (H-F) method [44–46] constructs the N-electron wave function Ψ^N as a single Slater determinant of N single-electron wave functions ψ [47, 48], which are self-consistently optimized such that they minimize the total energy of Ψ_N. The main limitation is that electron-electron interactions are accounted for only in a mean-field approximation, thus neglecting correlation effects [49, 50]. This problem can be alleviated by a number of different post-H-F methods [51], which are however without exception, computationally extremely costly and feasible only for very small molecules.

[2] As long as the molecule-substrate coupling is much stronger than the tip-molecule coupling, such that the molecule between tunneling events always returns to the N-electron state and no transitions involving ($N\pm m$)-electron states with $m>1$ are probed.

An alternative approach is density functional theory (DFT), which does not minimize the energy with respect to the many-electron wave function as H-F based methods but with respect to the electron density. DFT builds on two theorems, essentially stating that (i) the ground state energy E of a system of N electrons is a functional of the electron density $n(\mathbf{r})$ and (ii) for each system there exists a unique $n(\mathbf{r})$ such that E is minimized [52]. The total electron density is then decomposed into N non-interacting single-electron wave functions ψ, the so-called Kohn-Sham (KS) eigenstates [53]. Those KS states experience an effective potential, which includes the static potential due to the atomic nuclei, the electron-electron Coulomb repulsion and the many-particle interactions through an exchange-correlation (XC) functional. As the effective potential depends on $n(\mathbf{r})$, the KS eigenstates are self-consistently optimized until the energy reaches a minimum. While the method is mathematically exact and would yield the correct density and total energy, the difficulty arises from finding the correct XC functional. To date, no exact formulation of it exists but many different approximations, and results of DFT calculations can be highly sensitive to the functional used [54, 55].

Both the above methods, H-F and DFT, approximate the solution to the many-electron problem by a set of effective single-electron orbitals. However, in particular the KS eigenstates carry strictly speaking no physical meaning [54, 56], as they only constitute a mathematical construct (except the energy of the highest occupied KS state, which should correspond to the ionization potential according to the DFT version of the Koopmans theorem [57,58]). Nevertheless, it has become customary to directly interpret experimental STS spectra in a similar single-particle picture [13, 59, 60], where the peaks in the $\mathrm{d}I/\mathrm{d}V$ are usually assigned to the KS states denoting the highest occupied (HOMO-k) or lowest unoccupied (LUMO+k) molecular orbitals of the N-electron system. To make matters worse, DFT is a ground state theory but in STS, resonances beyond the frontier orbitals usually correspond to excited states. In the single-particle picture, those are simply obtained by occupying or unoccupying the orbitals of the ground state in the given order. However, in principle DFT is not sufficient to determine the elementary excitations [61].

One possible way of calculating excited states is an extension of DFT called time-dependent density functional theory (TDDFT) [62, 63]. Here, a small time-dependent perturbation is added to the effective potential. In the most common implementation of TDDFT, the many-body excited

states are then given by the poles of the linear response function of the charge density [64]. Such calculations are usually carried out in the so-called adiabatic approximation, where it is assumed that the XC functional reacts instantaneously and without memory to previous changes of the charge density [63]. The limitations of TDDFT lie then analogously to standard DFT in the approximations made in the XC functional.

2.2 Growth of hexagonal boron nitride by chemical vapour deposition

As stated in section 2.1, STM experiments are usually performed on atomically clean surfaces, requiring not just imaging but also sample preparations to be carried out in UHV. Thin films of h-BN can readily be grown in UHV by chemical vapour deposition (CVD). The basic principle of CVD is to expose a substrate to a vapour of precursors molecules, which decompose or react on the surface, often facilitated by supplying energy to the system in the form of heat or using a substrate that is catalytically active.

h-BN has been shown to grow on various transition metal surfaces upon thermal decomposition of the benzene-like borazine, $B_3N_3H_6$ [31, 65–74]. The process is usually self-limiting, as the catalytic activity of the substrate is required to crack the borazine. Once there is no free metal surface left, the growth process stops, conveniently resulting in exactly one monolayer (ML) of h-BN. If there is a lattice mismatch between the h-BN and the substrate, the registry between the boron and nitrogen atoms and the substrate atoms will vary in an alternating fashion, resulting in a periodic superstructure. If the substrate and overlayer both exhibit hexagonal symmetry, this so-called moiré pattern will have hexagonal symmetry as well, as shown in Fig. 2.4.

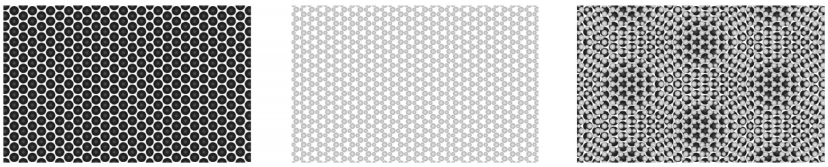

Figure 2.4. Formation of a moiré pattern: Overlaying two crystal lattices with different lattice constants (left and middle) results in a periodic variation of the interlayer registry (right).

The moiré periodicity λ can be derived from the reciprocal lattice vectors

[75] and depends on the relative lattice mismatch δ:

$$\lambda = \frac{(1+\delta)a}{\sqrt{2(1+\delta)(1-\cos\varphi)+\delta^2}} \quad , \tag{2.21}$$

where a is the periodicity of the overlayer, *i.e.* h-BN. Equation 2.21 reveals that the period also depends on the relative orientation between h-BN and the substrate, the maximum value of λ corresponding to the two lattices being aligned, *i.e.* $\varphi = 0$. For non-zero φ, there will be also an angle ϑ between the h-BN lattice and the moiré lattice, given by

$$\tan\vartheta = \frac{\sin\varphi}{1+\delta-\cos\varphi} \quad . \tag{2.22}$$

If φ is small, Eq. 2.22 can be simplified to the linear relationship $\vartheta = \varphi/\delta$, in which case ϑ will simply magnify the atomic misalignment between h-BN and the substrate.

The formation of different rotational domains poses a serious challenge to the growth of high-quality h-BN films. One way to minimize their occurrence is by the choice of the substrate, where one usually differentiates between weakly and strongly interacting substrates. While weakly interacting substrates offer the advantage that the electronic properties of h-BN are fully preserved, different adsorption configurations of h-BN on such surfaces vary little in energy and have thus similar formation probability during the growth [69, 72]. Prototypical examples are h-BN/Pt(111) [65] or h-BN/Cu(111) [72]. On strongly interacting substrates, on the other hand, there usually exists one adsorption configuration which is energetically strongly favoured, resulting in a preferred growth direction. However, this is often accompanied by strong hybridization of h-BN π states with d states of the substrate [67], potentially diminishing the insulating properties of h-BN. In addition, the interaction strength (weak - strong) also governs the corrugation (low - high) between different regions of the h-BN/metal moiré pattern. On the strongly interacting substrates Rh(111) [31] and Ru(0001) [66], the moiré corrugation is between 1 and 1.5 Å [76], while h-BN on Cu(111) is essentially flat [72]. Previous work indicates that Ir(111) might be right at the sweet point between the two extrema, *i.e.* sufficiently weakly interacting to preserve the insulating properties of h-BN while at the same time allowing for the growth of a single rotational domain [65, 72, 77].

The quality of the h-BN layer is further influenced by the growth conditions. There are two variations of the CVD method: the standard way is to heat the sample to the desired temperature and then expose the already hot substrate to the borazine. Alternatively, the surface can be kept

at room temperature (RT) while dosing in the precursor, which will adsorb on the surface (usually until the surface is saturated) and only then heat the sample to the growth temperature. This latter method is often referred to as temperature programmed growth (TPG) [78]. In principle, the growth then proceeds analogously, starting with dehydrogenation of borazine, cracking of the molecular ring into fragments and atomic boron and nitrogen and reorganization into small BN clusters, which then grow and coalesce to form the h-BN layer [68,70,74]. However, the crystallinity of the layer will strongly depend on the growth method and chosen temperature [73,74]. TPG leads to a high nucleation density, since the surface is fully covered with molecules or their fragments as the temperature reaches the thresholds for thermal decomposition and cluster formation, respectively. For lattice-mismatched systems, it is then very unlikely for different h-BN islands to coalesce coherently [68,74]. If all domains are rotational aligned, Eq. 2.21 yields for h-BN (a=2.505 Å [79]) on Ir(111) (a=2.714 Å [80]) a moiré period of 32.5 Å, which would correspond to a 13×13-on-12×12 unit cell. Thus, there are already 144 translational domain just for aligned h-BN [68], with an accordingly inverse probability for two domains to merge coherently. As a result, TPG often leads to a mosaic-like growth where the final overlayer is polycrystalline with a small domain size (Fig. 2.7a). Higher temperatures or longer heating times will usually result in larger islands [78].

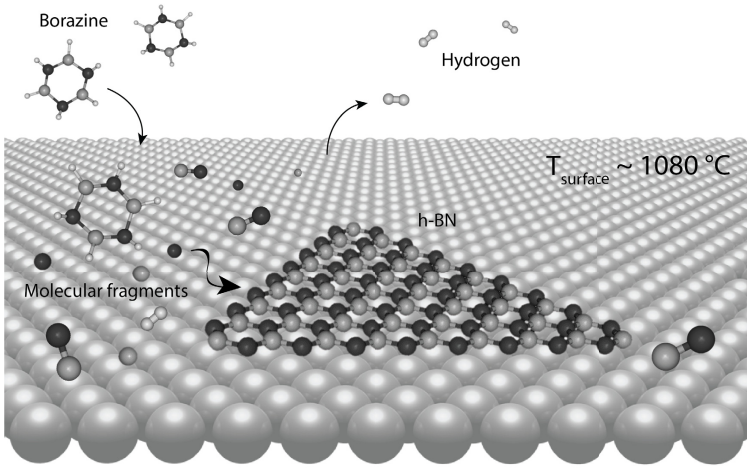

Figure 2.5. Schematic of chemical vapour deposition growth of h-BN. Borazine precursor molecules decompose on a hot surface (e.g. for Ir(111) 1080 °C) and the fragments form the h-BN monolayer.

This situation can be avoided in standard CVD: the nucleation density

depends on the ratio between deposition flux and surface diffusion [68], which thus can be minimized by a low partial pressure of the introduced precursor and a high growth temperature. This approach is also called low-pressure high-temperature CVD (LPHT-CVD) and can lead to nucleation densities in the order of one per μm^2 [68, 78], as shown in Fig. 2.6. The h-BN islands also overgrow step-edges in a carpet-like fashion [74, 81], allowing for formation of single domains up to several μm^2 in size [71]. For Ir(111), the maximum h-BN growth temperature is between 1000 and 1100 °C [70, 73]. At higher temperatures the h-BN layer decomposes, whereby atomic boron likely diffuses into the bulk and nitrogen desorbs as NH_x or N_2 [70, 73, 82].

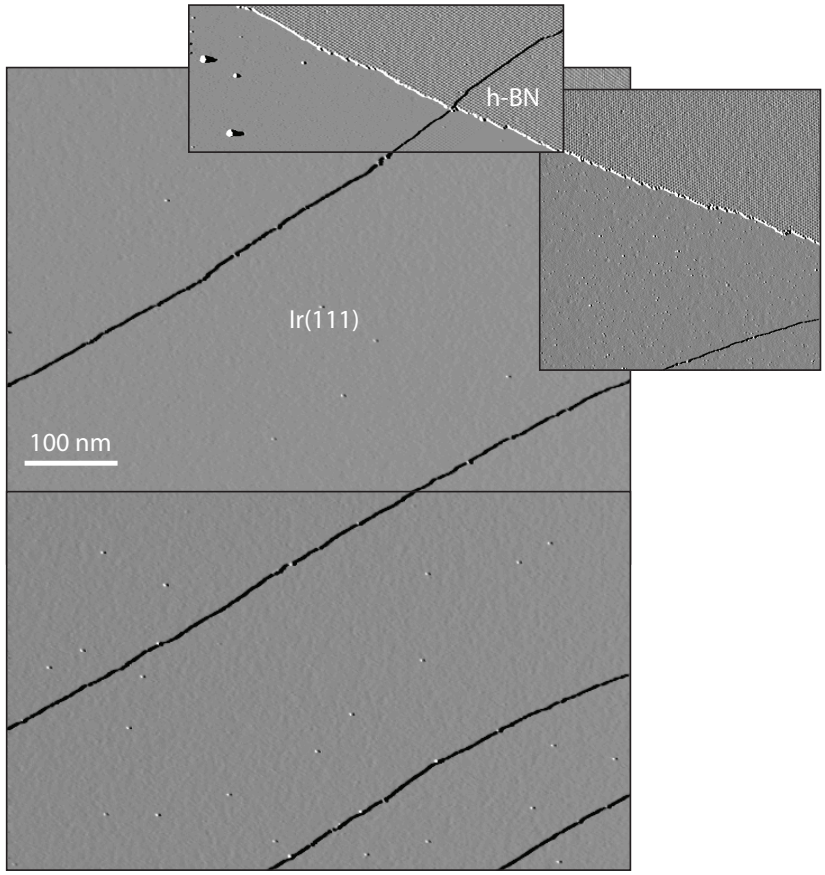

Figure 2.6. Growth of h-BN on Ir(111) by low-pressure high-temperature CVD ($p_{B_3N_3H_6}$ = 2×10^{-8} mbar, $T_{Ir(111)}$ = 1080 ° C, t_{growth} = 4.5 min). The four STM images show a total unique area of 0.66 μm^2 with a single h-BN islands growing at the top right corner, yielding as an estimation of the upper limit of the nucleation density on that sample 1.5 μm^{-2}.

All the above considerations apply similarly to the CVD growth of graphene on Ir(111) [75, 78]. Here, ethylene is commonly used as precursor

molecule, which decomposes *via* various intermediates into atomic carbon and subsequently forms carbon clusters and then ordered graphene islands [78, 83, 84]. One difference is that graphene can be grown at even higher temperatures, being stable still at 1500 °C [73] (probably due to the lower solubility in iridium of carbon compared to boron [82]).

Both h-BN and graphene islands grow with zigzag (ZZ) edges [74, 85], but for h-BN this has an interesting consequence. Due to the interaction with the substrate, one of the two inequivalent ZZ edges (either boron- or nitrogen-terminated) is energetically more favourable - according to DFT calculations for Ru(0001) the nitrogen edge [74]. The preferred island shape then will be triangular (Figs. 2.7a and b), as the occurrence of the energetically less favourable edge is minimized during growth. On the contrary, the graphene islands shown in Fig. 2.7c show mostly a hexagonal shape. Due to the slightly larger lattice constant of G, its moiré pattern on Ir(111) (Fig. 2.7d) has a shorter periodicity of ~ 25 Å [75].

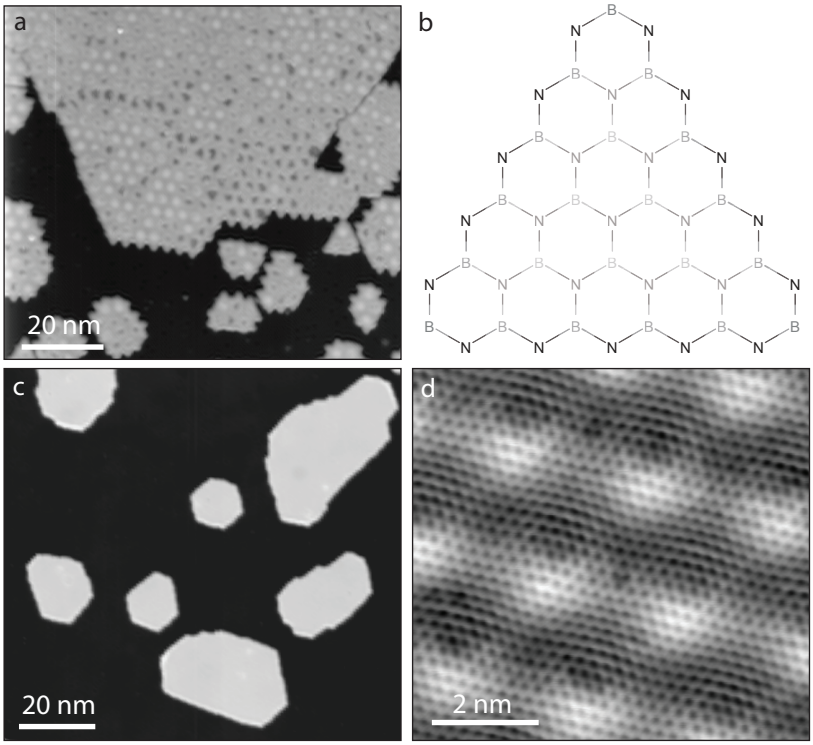

Figure 2.7. (a) h-BN grown on Ir(111) by TPG (surface fully covered with borazine at RT and flashed to 1000 °C). (b) Triangular shapes of h-BN islands minimize the occurrence of one of the two inequivalent ZZ edges, in this example boron-terminated edges. (c) Graphene grown on Ir(111) by TPG (surface fully covered with ethylene at RT and flashed to 1300 °C). (d) G/Ir(111) moiré pattern.

2.3 Set-up

All experiments for publications PI, PII and PIII were performed on a commercial CreaTec LT-STM/AFM (www.createc.de) with PAN-type slider, shown in Fig. 2.8 and operated at 5 K and under UHV conditions (base pressure 10^{-10} mbar). The only significant modification of the system is the addition of low-pass filters for the voltage signals driving the piezo scanner in x, y (1 kHz, 2nd order) and z (1 kHz, 1st order) direction. A preparation chamber for sample cleaning, chemical vapour deposition and evaporation of molecules is housed within the same UHV system, allowing for sample transfer into the microscope without breaking the vacuum.

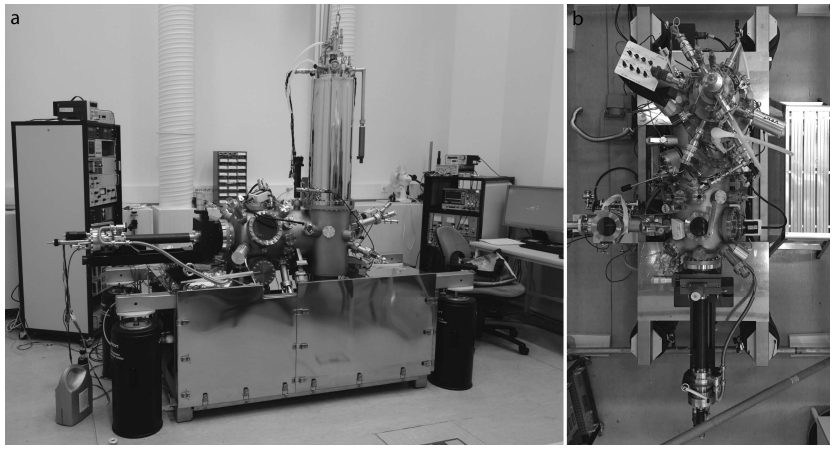

Figure 2.8. (a) Side and (b) top view of the CreaTec LT-STM/AFM used for most of the experiments presented in this thesis.

Experiments for publication PIV were mostly performed on a commercial Unisoku USM1300 low-temperature STM (www.unisoku.com), operated at 5 K and under UHV conditions as well.

Ir(111) single crystals, used as a substrate for all experiments presented in this thesis, were cleaned by repeated cycles of sputtering with 1.5 keV neon ions, annealing to 900 °C in 5×10^{-7} mbar oxygen and subsequent flashing to 1400 °C. Further details can be found in the corresponding sections of the original publications.

3. Results

3.1 The structure of h-BN on Ir(111)

Publication PI investigated the atomic scale structure and electronic properties of h-BN on Ir(111). To ensure a high quality of the h-BN, it was grown by low-pressure high-temperature CVD at a borazine pressure of 2×10^{-8} mbar and sample temperature of 1080 °C. A large scale STM image in Fig. 3.1a shows a single h-BN domain extending over several monatomic substrate steps. The moiré superstructure (Fig. 3.1b) is formed by depressions arranged in a hexagonal lattice, which for historical reasons [31, 65] will be referred to throughout this thesis as 'pores', while the region surrounding them as 'wires'. Figure 3.1b also reveals that the angle between the h-BN and the moiré lattices is negligibly small, indicative of an overlayer which is aligned with the Ir substrate (Eq. 2.22). The experimentally determined moiré periodicity of (29.3±0.6) Å is slightly reduced compared to the theoretical value of 32.5 Å (Eq. 2.21), suggesting that the h-BN layer is strained by 0.8% [86, 87].

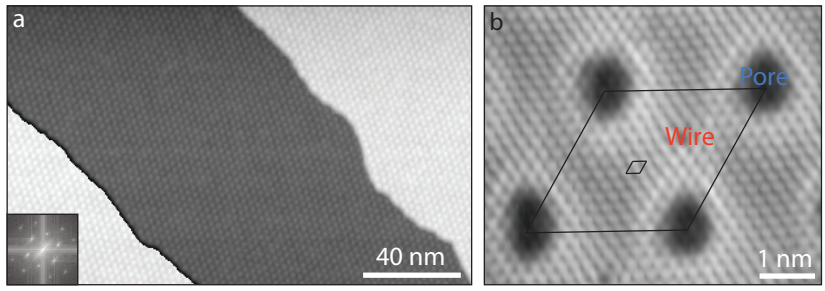

Figure 3.1. (a) Large-scale STM image of an h-BN domain grown on Ir(111) and extending over two monatomic steps. Inset: Fast-Fourier transform confirming the single-crystalline nature of the h-BN domain and its hexagonal symmetry. (b) Atomically resolved image of the moiré pattern, with pore and wire regions marked.

According to the DFT calculations[1] shown in Fig. 3.2a, the pore regions correspond to N atoms occupying Ir(111) top sites and B atoms hcp hollow sites ($N_{top}B_{hcp}$), where a large overlap between N p states and Ir d states results in a lower adsorption height. The largest adsorption height of the h-BN layer corresponds to both species occupying hollow sites ($N_{hcp}B_{fcc}$), with a total corrugation of 35 pm.[2] The DFT projected density of states of the B and N p_z component depicted in Fig. 3.2b also suggest that the strong interaction of the h-BN layer with the substrate on the pores leads to a local downward shift of its conduction band. This finding is supported by the STM contrast reversal on the moiré, with the pores appearing as protrusions at large positive bias. Nevertheless, the PDOS in the h-BN gap is very low, suggesting that it should be able to serve as a decoupling layer.

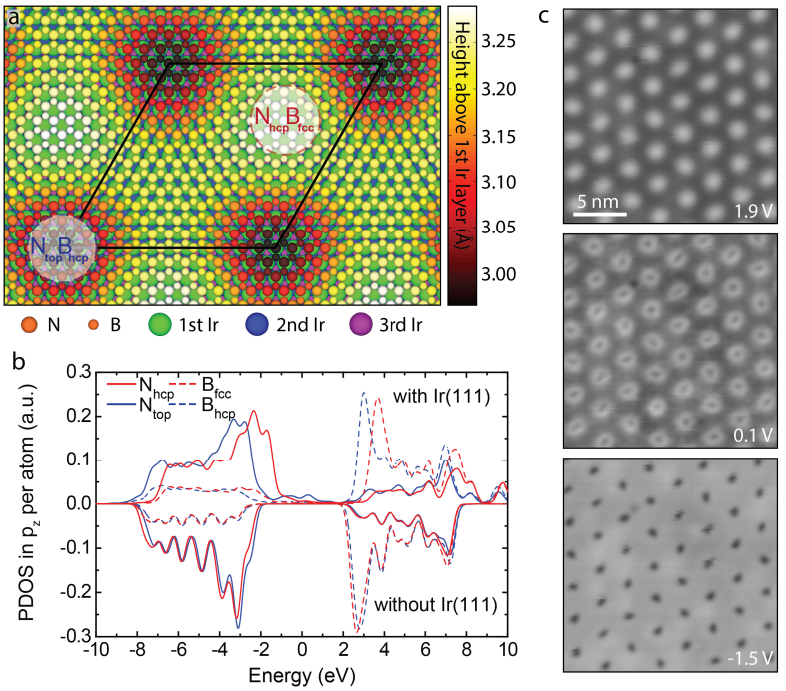

Figure 3.2. (a) DFT-optimized structure of the h-BN/Ir(111) moiré. (b) Projected density of states for atoms in the two regions marked in (a). (c) Bias voltage-dependent STM image contrast of the moiré.

[1]All DFT calculations presented in this thesis have been carried out using the generalized gradient approximation to the XC functional as parametrized by Perdew, Burke and Ernzerhof (PBE) [88] or its revised version (revPBE) [89]. Please see the original articles in the *Publications* sections for computational details.

[2]This value is slightly dependent on the XC functional and how dispersion forces are treated [90].

The moiré also modulates the local work function of the h-BN layer: Fig. 3.3b shows measurements of the tunneling current as a function of the tip-sample distance for different parts of the sample (crosses in Fig. 3.3a). The decay constant on the pore is smaller than on the wire or the clean Ir(111), indicating a lowering of the work function (Eq. 2.1). This can also be visualized through field emission resonances (FERs), whose origin is depicted in Fig. 3.3c: When the bias voltage exceeds the sample work function, a trapezoidal potential between tip and surface is formed, giving rise to hydrogen-like electronic resonances [91–93]. These resonances can be measured by STS with a closed current feedback and a set of such spectra taken along a high-symmetry line of the moiré (arrow in Fig. 3.3a) is shown in Figs. 3.3d and e. Since their energy depends on the sample work function [94], they allow for an estimation of the spatial variation of the surface potential [95–97]. Combining the results from $I(z)$ [98] and FER measurements, the local work function on the pores is roughly 0.5 eV lower compared to its highest value on the wire regions. This spatial variation of the work function is in good agreement with values of the Hartree potential extracted from DFT calculations (Fig. 3.3f) and can be explained by the different hybridization strength between h-BN and Ir(111) over the moiré unit cell [99–101].

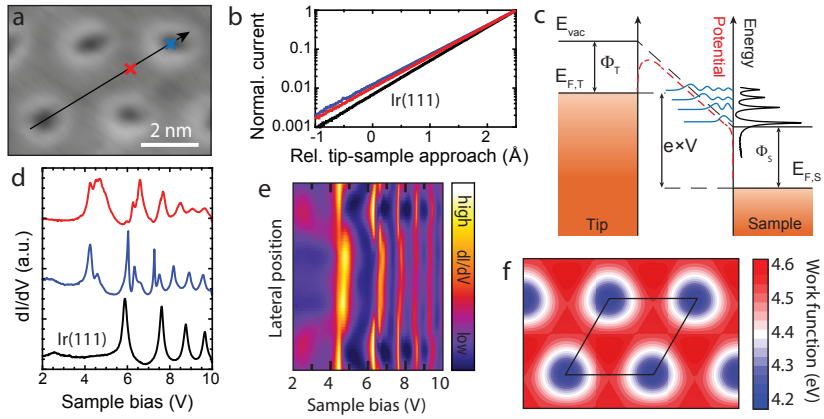

Figure 3.3. (a) STM image marking the location of the $I(z)$ and FER spectra. (b) $I(z)$ measurements on the pore (blue) and wire (red) regions and on the clean Ir(111) (black). (c) Schematic of FERs formed in the trapezoidal potential well between tip and sample when the bias voltage exceeds the sample work function. (d) Same as (b) but for FER spectra. (e) False color plot of a series of FER spectra taken along the arrow shown in panel (f). (e) Local work function over the h-BN moiré unit cell calculated from DFT.

3.2 Single-molecule tunneling spectroscopy on h-BN

Publications PII and PIII explored the possibilities of monolayer h-BN on Ir(111) to serve as ultra-thin insulating layer for tunneling spectroscopy on single molecules. As a model system, we used the well-studied cobalt phthalocyanine (CoPC) [102–104], a dye molecule consisting of an aromatic macrocycle which coordinates a cobalt atom in its central cavity.

PII focussed on the effect of the h-BN moiré on the self-assembly and electronic structure of CoPC. Figures 3.4b and c show the sample at two different submonolayer coverages of CoPC. At low coverages (panel b), the molecules exclusively adsorb on the moiré pores, due to the stronger interaction with the metal substrate and the electric field caused by the change of the work function [105], in agreement with previous studies [106, 107]. Only once all the pores are occupied, the molecules also decorate the wire regions (panel c).

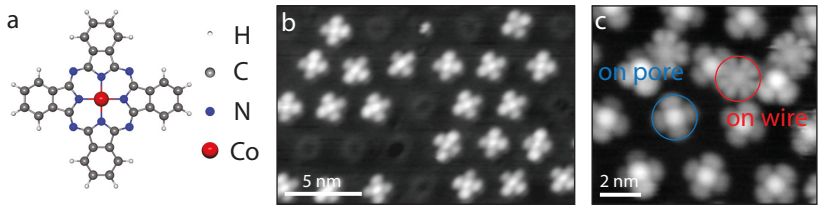

Figure 3.4. (a) Structural model of cobalt phthalocyanine. (b) h-BN/Ir(111) at low CoPC coverage, when the molecules exclusively adsorb on the pores. (c) At higher coverages, CoPC also adsorbs on the wires.

Interestingly, CoPCs exhibit different intramolecular contrast in STM images, depending on whether they adsorb on the wire or the pore. This is a clear indication that the h-BN moiré modulates the molecule's electronic properties, which is confirmed by the STS measurements shown in Figs. 3.5a and b. The dI/dV for molecules on the wire (panel a) shows that the lowest transition at positive bias for electron injection is localized at the cobalt center (labeled N2), the second one is delocalized over the macrocycle (N1) and for electron removal at negative bias, the first transition is also delocalized (N3). On the pore (panel b), the lowest transition at positive bias is a delocalized state (A1), while at negative bias the first transition appears on the cobalt center (A2) and two further transitions are delocalized over the molecule's macrocycle (A3, A4). Comparison between STM images at different bias voltages depicted in Fig. 3.5c and previous studies [103, 104] suggests that CoPC on the wire is in a neutral ground state ($CoPC^0$). On the pore, the molecules are negatively charged

and in an anionic ground state ($CoPC^{-1}$), as the lowest unoccupied state of the neutral species shifts below the substrate Fermi level due to the lower work function [108].

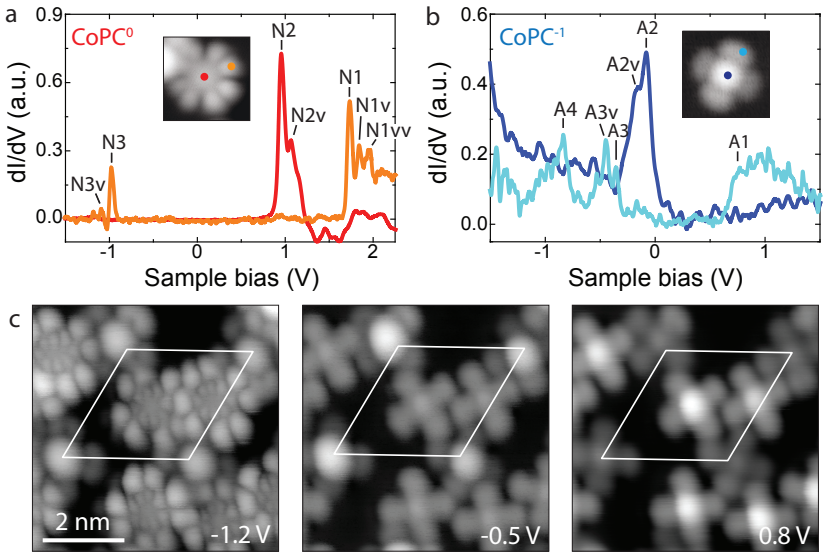

Figure 3.5. (a) dI/dV spectra for CoPC adsorbed on the wire, where it remains in a neutral ground state. (b) Same for CoPC on the pore, where it gets negatively charged. (c) STM images of CoPC/h-BN/I(111) at different bias voltages, showing how the metal-centered lowest unoccupied molecular state on the wire shifts to below the Fermi level on the pore.

Two further important observations can be made from the dI/dV in Fig. 3.5: (i) all the transitions exhibit satellite peaks (labeled N1v, N1vv, A2v and so on). Their constant spacing of ∼100 mV [109] identifies them as vibronic replica [110, 111] due to additional excitation of molecular vibrations as the electron tunnels resonantly through the CoPC. (ii) the resonances are very narrow and Lorentzian shaped, with an average line width of ∼37 mV (N2) on the wire and ∼60 mV (A2) on the pore [109]. Both (i) and (ii) indicate that the molecules on the h-BN are well-decoupled from the underlying Ir substrate, even though on the pores the h-BN is less insulating due to the stronger interaction with the metallic substrate. In addition, (ii) represents a significant advantage over the commonly used alkali halides, where coupling of the molecular resonances with optical phonons of the insulating layers leads to broad, Gaussian-shaped peaks [20, 27].

PIII continued with a more detailed investigation of the observed resonances and went beyond the prevalent singe-particle (SP) picture of STS. Here, one would expect that the negative charging of CoPC on the pore

would lead to a downward shift in energy of all the observed transitions (3.5a and b). This seems to hold true for A1 and A2, which could be interpreted as N1 and N2 shifted down by ∼1 V. However, transition A3 of $CoPC^{-1}$ - in the SP picture corresponding to N3 of $CoPC^{0}$ - should then appear well below -1.0 V. Instead, there are two transitions A3 and A4 just below A2 at energies of ∼-0.3 and ∼-0.8 V, respectively. In addition, maps of the spatial variation of the dI/dV signal shown in Fig. 3.6 reveal that the wave functions corresponding to transitions N3 and A3 exhibit a different shape and symmetry, in contrast to the expected behaviour based on the SP picture.

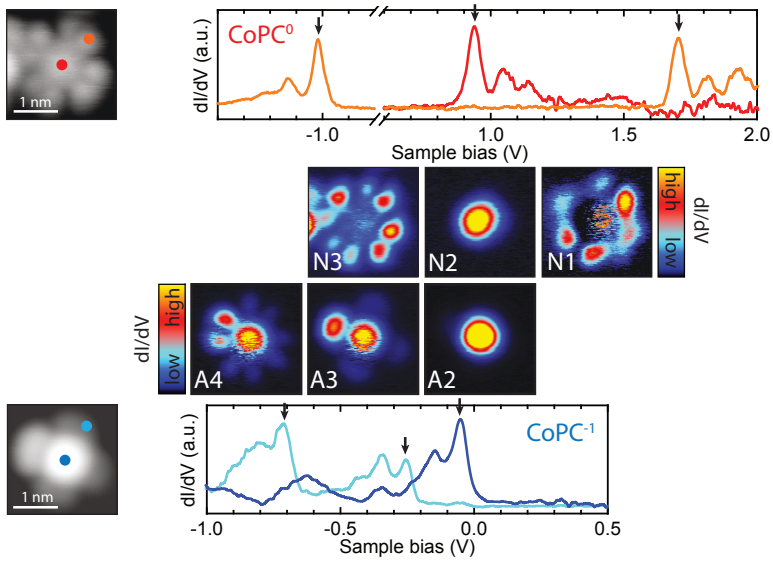

Figure 3.6. High-resolution STS and corresponding dI/dV maps, revealing that the orbital order for $CoPC^{0}$ and $CoPC^{-1}$ is different.

According to section 2.1.3 and Eq. 2.20, resonances A3 and A4 at negative bias correspond to transitions into N-electron excited states $|\Psi_k^N\rangle$ (electron removal from $CoPC^{-1}$), which in the SP picture would be obtained by simply unoccupying the single-particle states (e.g. Kohn-Sham states from DFT) of the molecule's ground state in their respective order. However, this neglects many-body (MB) effects due to the interaction of the hole with the remaining electrons, which can result in orbital re-ordering and mixing of multiple single-particle excitations. Such effects can be taken into account by using TDDFT to explicitly calculate the many-body excited states of the molecule and project them onto a chosen set of SP orbitals, in our case the KS orbitals of neutral CoPC. Figure 3.7a compares the dominant contributions to the first three MB excited

states for electron removal from $CoPC^{-1}$ with the SP excited states and the experimental dI/dV maps. Identifying transitions A3 and A4 with the first and second MB excited states, it can be seen that the observed orbital re-ordering is well-described by the excited states computed from TDDFT. Figure 3.7b makes a similar comparison for electron injection into $CoPC^{0}$, according to which transition N1 can be interpreted as the second MB excited state of the $(N+1)$-electron state, while the fifth MB excited state could explain the extra intensity of the second vibronic replica N1vv (intensities of vibronic replica should follow a Poison distribution [111], according to which N1vv should have much lower intensity than N1v). Here, the first, third and fourth MB excited state are not expected to be visible in STS, as their dominant contribution requires an additional intramolecular transition [112].

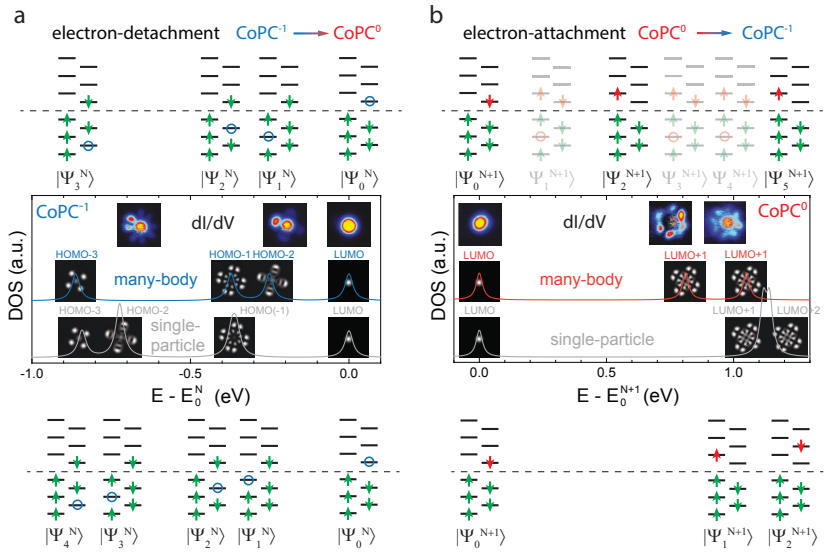

Figure 3.7. Comparison of the single-particle (excited states from ground state DFT) and many-body (excited states from TDDFT) picture with the experimental data for (a) electron removal from $CoPC^{-1}$ and (b) electron injection into $CoPC^{0}$. For the TDDFT excited states, only the dominant contributions upon projection onto the KS orbitals are shown.

3.3 Electronic states at the h-BN/graphene interface

In PIV, we expand on the usual idea of using ultra-thin insulating layers to decouple molecules and instead, grow in-plane heterostructures of hexagonal boron nitride and graphene (h-BN/G) to decouple the G edges from the metallic substrate. Theory predicts that zigzag edges of G should

host a one-dimensional, non-dispersive electronic state [113–115], which has attracted considerable interest due to its predicted exotic properties, such as spin-polarization [114, 116]. However, the experimental realization of this state faces two challenges: the G ZZ edges should be (i) atomically perfect and straight without disorder to minimize scattering and (ii) passivated to avoid quenching of the state through chemical functional groups or interaction with the substrate. Most approaches of achieving G edges overcome only one of these two obstacles [117–119].

TPG-grown G on Ir(111) readily achieves (i), with the length of straight ZZ segments limited only by the moiré superstructure (section 2.2), but the strong interaction of the edge with the metallic substrate quenches the edge state [119]. This problem is circumvented by covalently attaching h-BN to the G edges in a second CVD step. The different moiré superstructures for h-BN and G on Ir(111) [75, 101] can cause reconstructions at the interface, which are reduced by intercalating the h-BN/G interfaces with several monolayers of the weakly interacting gold [120, 121]. An overview STM image of such a sample in Fig. 3.8a shows G islands with small h-BN attachments, either adsorbed on top or embedded in the top-most layer of the Au(111) film, which shows its characteristic herringbone reconstruction [122].

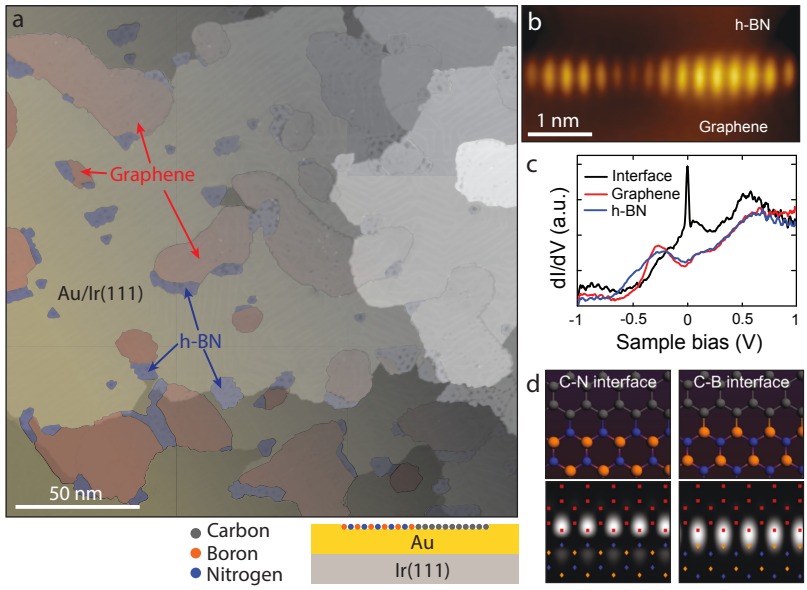

Figure 3.8. (a) Overview STM image of h-BN/G interfaces grown on Ir(111) and intercalated with gold. (b) Zoom-in on one of the interfaces, exhibiting a characteristic lobe structure. (c) dI/dV spectrum taken at the interface, revealing a narrow peak close the zero bias voltage. (d) DFT simulation of the tunneling current over a boron- and nitrogen-terminated h-BN/G interface.

Figure 3.8b is a zoom-in STM image onto one of the h-BN/G interfaces, where a prominent series of elongated lobes is visible. STS (Fig. 3.8c) reveals a narrow resonance close to zero bias voltage, localized directly at the interface and absent from spectra taken on either G or h-BN. DFT simulations of the h-BN/G interface shown in Fig. 3.8d do not just confirm that the observed electronic state is indeed a property of the interface itself, but also suggest that the h-BN is boron-terminated at the interface.

In Fig. 3.9, band structures from tight-binding calculations for a G nanoribbon with clean [123] (panel a) and BN-terminated [124] (panel b) ZZ edges are compared. The initially non-dispersive edge state bends down by ΔE between the K and K' points due to the bonding with the boron atoms. However, the narrow peak in the dI/dV spectrum (Fig. 3.8c) shows that in our case, ΔE is very small, indicating that the interface state formed after passivating the G edge with h-BN closely resembles the pure graphene zigzag edge state.

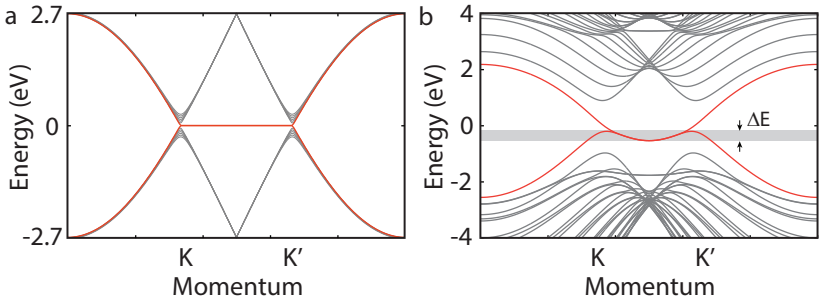

Figure 3.9. Tight-binding band structures for a pristine (a) and h-BN-terminated (C-B interface) graphene zigzag ribbon. Red marks the edge and interface state, respectively. The difference in the bulk bands (gray) us due to the different size of the calculated ribbons. Panel (a) adapted with permission from ref. [123]. Copyright by the American Physical Society.

4. Summary and Outlook

This thesis explored the possibilities to utilize h-BN as an ultra-thin insulating layer for STS. Monolayer h-BN was grown on Ir(111) and characterized by STM, showing that it can be grown with high quality and long-range structural coherence. The Ir(111) surface has attracted considerable interest in recent years as G on Ir(111) emerged as the quasi-gold standard for CVD graphene [81, 125]. Its interaction is weak enough to preserve the linear dispersion of G around the Fermi energy, while still facilitating single-domain growth. These observations motivated several groups to study also h-BN growth and its optimization on Ir(111) [70, 73, 126], and this work adds a local probe perspective to the existing literature. In addition, STS measurements of the work function along the h-BN/Ir(111) moiré revealed a periodic variation of roughly 0.5 eV, demonstrating how slight variations in the hybridization of h-BN and Ir states can have a strong influence on the local electronic structure.

STS experiments on CoPC molecules adsorbed on h-BN/Ir(111) demonstrated that the insulating nature of h-BN is nevertheless preserved: Narrow, Lorentzian shaped molecular resonances were observed, suggesting life time effects as the dominant broadening mechanism. This presents an important step forward, as the predominantly used metal oxides and alkali halides yield broad Gaussian shaped molecular resonances due to coupling with optical phonons of the insulating layer [27]. This broadening mechanism is essentially layer-thickness independent [27], thus limiting the energy resolution obtainable on such thin films. h-BN/Ir(111) offers the possibility to further reduce the line width and thus resolution through h-BN multilayers, which can be grown from solid boron sources [127].

The work function modulation on h-BN/Ir(111) leads to a local charging of CoPC, which enabled the measurements of its electronic properties as a

function of charge state. Comparing STS data for the two different species revealed inconsistencies with the prevalent single-particle interpretation of STS, which could be explained on the basis of many-body excited states calculated from TDDFT. These results are an important reminder that STS also probes excited states and those are generally not well-described by standard DFT [61] or Hartree-Fock calculations [128].

Going beyond the usual applications of ultra-thin insulating layers, the edges of CVD-grown graphene were decoupled from the metallic substrate by covalently attaching h-BN. The resulting electronic state at the interface strongly resembles the theoretically predicted edge state of pristine graphene [123], potentially opening up a new route to study some of the exotic effects linked to this state.

During the last few years, the literature on STM/STS using h-BN as ultra-thin insulator has grown markedly, with several publications investigating the effect of the h-BN/metal moiré onto the electronic structure of adsorbed molecules [129–133]. Additionally, h-BN was employed as decoupling layer for spin-flip spectroscopy [134]. In conjunction with those studies, this thesis demonstrates the versatility of h-BN as decoupling layer, allowing for detailed investigations of the electronic structure of adsorbates while also providing templating capabilities.

References

[1] I.-W. Lyo and P. Avouris, "Negative differential resistance on the atomic scale: implications for atomic scale devices," *Science*, vol. 245, no. 4924, pp. 1369–1371, 1989.

[2] B. C. Stipe, M. A. Rezaei, and W. Ho, "Single-molecule vibrational spectroscopy and microscopy," *Science*, vol. 280, no. 5370, pp. 1732–1735, 1998.

[3] C. Krull, R. Robles, A. Mugarza, and P. Gambardella, "Site- and orbital-dependent charge donation and spin manipulation in electron-doped metal phthalocyanines," *Nat. Mater.*, vol. 12, no. 4, pp. 337–343, 2013.

[4] N. Nilius, T. M. Wallis, and W. Ho, "Development of one-dimensional band structure in artificial gold chains," *Science*, vol. 297, no. 5588, pp. 1853–1856, 2002.

[5] D. Serrate, P. Ferriani, Y. Yoshida, S.-W. Hla, M. Menzel, K. von Bergmann, S. Heinze, A. Kubetzka, and R. Wiesendanger, "Imaging and manipulating the spin direction of individual atoms," *Nat. Nano.*, vol. 5, no. 5, pp. 350–353, 2010.

[6] M. Ruby, F. Pientka, Y. Peng, F. von Oppen, B. W. Heinrich, and K. J. Franke, "Tunneling processes into localized subgap states in superconductors," *Phys. Rev. Lett.*, vol. 115, no. 8, p. 087001, 2015.

[7] G. Binnig and H. Rohrer, "Scanning tunneling microscopy," *Helv. Phys. Acta*, vol. 55, no. 6, pp. 726–735, 1982.

[8] D. M. Newns, "Self-consistent model of hydrogen chemisorption," *Phys. Rev.*, vol. 178, no. 3, pp. 1123–1135, 1969.

[9] J. K. Nørskov, "Chemisorption on metal surfaces," *Rep. Progr. Phys.*, vol. 53, no. 10, p. 1253, 1990.

[10] P. Lazić, V. Caciuc, N. Atodiresei, M. Callsen, and S. Blügel, "First-principles insights into the electronic and magnetic structure of hybrid organic-metal interfaces," *J. Phys.: Cond. Matt.*, vol. 26, no. 26, p. 263001, 2014.

[11] C. Uhlmann, *Rastertunnelmikroskopie an Phthalocyanin-Molekülen auf ultradünnen Isolatorfilmen: Ladungszustand, Jahn-Teller Effekt und ein molekularer Schalter*. PhD thesis, Universität Regensburg, 2013.

[12] S. Schintke and W.-D. Schneider, "Insulators at the ultrathin limit: electronic structure studied by scanning tunnelling microscopy and scanning tunnelling spectroscopy," *J. Phys.: Cond. Matt.*, vol. 16, no. 4, p. R49, 2004.

[13] J. Repp, G. Meyer, S. M. Stojković, A. Gourdon, and C. Joachim, "Molecules on insulating films: Scanning-tunneling microscopy imaging of individual molecular orbitals," *Phys. Rev. Lett.*, vol. 94, no. 2, p. 026803, 2005.

[14] A. J. Heinrich, J. A. Gupta, C. P. Lutz, and D. M. Eigler, "Single-atom spin-flip spectroscopy," *Science*, vol. 306, no. 5695, pp. 466–469, 2004.

[15] M. Sterrer, T. Risse, U. Martinez Pozzoni, L. Giordano, M. Heyde, H.-P. Rust, G. Pacchioni, and H.-J. Freund, "Control of the charge state of metal atoms on thin MgO films," *Phys. Rev. Lett.*, vol. 98, no. 9, p. 096107, 2007.

[16] J. Repp, G. Meyer, F. E. Olsson, and M. Persson, "Controlling the charge state of individual gold adatoms," *Science*, vol. 305, no. 5683, pp. 49–495, 2004.

[17] S. W. Wu, N. Ogawa, G. V. Nazin, and W. Ho, "Conductance hysteresis and switching in a single-molecule junction," *J. Phys. Chem. C*, vol. 112, no. 14, pp. 5241–5244, 2008.

[18] T. Leoni, O. Guillermet, H. Walch, V. Langlais, A. Scheuermann, J. Bonvoisin, and S. Gauthier, "Controlling the charge state of a single redox molecular switch," *Phys. Rev. Lett.*, vol. 106, no. 21, p. 216103, 2011.

[19] X. H. Qiu, G. V. Nazin, and W. Ho, "Vibronic states in single molecule electron transport," *Phys. Rev. Lett.*, vol. 92, no. 20, p. 206102, 2004.

[20] N. Pavliček, I. Swart, J. Niedenführ, G. Meyer, and J. Repp, "Symmetry dependence of vibration-assisted tunneling," *Phys. Rev. Lett.*, vol. 110, no. 13, p. 136101, 2013.

[21] J. Repp, P. Liljeroth, and G. Meyer, "Coherent electron-nuclear coupling in oligothiophene molecular wires," *Nat. Phys.*, vol. 6, no. 12, pp. 975–979, 2010.

[22] S. Schintke, S. Messerli, M. Pivetta, F. Patthey, L. Libioulle, M. Stengel, A. De Vita, and W.-D. Schneider, "Insulator at the ultrathin limit: MgO on Ag(001)," *Phys. Rev. Lett.*, vol. 87, no. 27, p. 276801, 2001.

[23] X. Lin, N. Nilius, H.-J. Freund, M. Walter, P. Frondelius, K. Honkala, and H. Häkkinen, "Quantum well states in two-dimensional gold clusters on MgO thin films," *Phys. Rev. Lett.*, vol. 102, no. 20, p. 206801, 2009.

[24] T. Bertrams, A. Brodde, and H. Neddermeyer, "Tunneling through an epitaxial oxide film: Al_2O_3 on NiAl(110)," *J. Vac. Sci. & Tech. B*, vol. 12, no. 3, pp. 2122–2124, 1994.

[25] N. Nilius, T. M. Wallis, and W. Ho, "Influence of a heterogeneous Al_2O_3 surface on the electronic properties of single Pd atoms," *Phys. Rev. Lett.*, vol. 90, no. 4, p. 046808, 2003.

[26] K. Glöckler, M. Sokolowski, A. Soukopp, and E. Umbach, "Initial growth of insulating overlayers of NaCl on Ge(100) observed by scanning tunneling microscopy with atomic resolution," *Phys. Rev. B*, vol. 54, no. 11, pp. 7705–7708, 1996.

[27] J. Repp, G. Meyer, S. Paavilainen, F. E. Olsson, and M. Persson, "Scanning tunneling spectroscopy of Cl vacancies in NaCl films: Strong electron-phonon coupling in double-barrier tunneling junctions," *Phys. Rev. Lett.*, vol. 95, no. 22, p. 225503, 2005.

[28] A. Zunger, A. Katzir, and A. Halperin, "Optical properties of hexagonal boron nitride," *Phys. Rev. B*, vol. 13, no. 12, pp. 5560–5573, 1976.

[29] K. Karch and F. Bechstedt, "Ab initio lattice dynamics of BN and AlN: Covalent versus ionic forces," *Phys. Rev. B*, vol. 56, no. 12, pp. 7404–7415, 1997.

[30] N. Ooi, A. Rairkar, L. Lindsley, and J. B. Adams, "Electronic structure and bonding in hexagonal boron nitride," *J. Phys.: Cond. Matt.*, vol. 18, no. 1, p. 97, 2006.

[31] M. Corso, W. Auwärter, M. Muntwiler, A. Tamai, T. Greber, and J. Osterwalder, "Boron nitride nanomesh," *Science*, vol. 303, no. 5655, pp. 217–220, 2004.

[32] A. Preobrajenski, A. Vinogradov, and N. Mårtensson, "Monolayer of h-BN chemisorbed on Cu(111) and Ni(111): The role of the transition metal 3d states," *Surf. Sci.*, vol. 582, no. 1–3, pp. 21–30, 2005.

[33] F. Müller, K. Stöwe, and H. Sachdev, "Symmetry versus commensurability: Epitaxial growth of hexagonal boron nitride on Pt(111) from B-trichloroborazine $(ClBNH)_3$," *Chem. Mater.*, vol. 17, no. 13, pp. 3464–3467, 2005.

[34] R. Laskowski, P. Blaha, T. Gallauner, and K. Schwarz, "Single-layer model of the hexagonal boron nitride nanomesh on the Rh(111) surface," *Phys. Rev. Lett.*, vol. 98, no. 10, p. 106802, 2007.

[35] A. K. Geim and K. S. Novoselov, "The rise of graphene," *Nat. Mater.*, vol. 6, no. 3, pp. 183–191, 2007.

[36] S. Bose, A. M. Garcia-Garcia, M. M. Ugeda, J. D. Urbina, C. H. Michaelis, I. Brihuega, and K. Kern, "Observation of shell effects in superconducting nanoparticles of Sn," *Nat. Mater.*, vol. 9, no. 7, pp. 550–554, 2010.

[37] S. Kahle, Z. Deng, N. Malinowski, C. Tonnoir, A. Forment-Aliaga, N. Thontasen, G. Rinke, D. Le, V. Turkowski, T. S. Rahman, S. Rauschenbach, M. Ternes, and K. Kern, "The quantum magnetism of individual manganese-12-acetate molecular magnets anchored at surfaces," *Nano Lett.*, vol. 12, no. 1, pp. 518–521, 2012.

[38] G. Binnig, H. Rohrer, C. Gerber, and E. Weibel, "7×7 reconstruction on Si(111) resolved in real space," *Phys. Rev. Lett.*, vol. 50, no. 2, pp. 120–123, 1983.

[39] J. Bardeen, "Tunnelling from a many-particle point of view," *Phys. Rev. Lett.*, vol. 6, no. 2, pp. 57–59, 1961.

[40] C. J. Chen, *Introduction to scanning tunneling microscopy*. Oxford University Press, 2. ed., 2008.

[41] J. Tersoff and D. R. Hamann, "Theory and application for the scanning tunneling microscope," *Phys. Rev. Lett.*, vol. 50, no. 25, pp. 1998–2001, 1983.

[42] J. Tersoff and D. R. Hamann, "Theory of the scanning tunneling microscope," *Phys. Rev. B*, vol. 31, no. 2, pp. 805–813, 1985.

[43] M. Ijäs, M. Ervasti, A. Uppstu, P. Liljeroth, J. van der Lit, I. Swart, and A. Harju, "Electronic states in finite graphene nanoribbons: Effect of charging and defects," *Phys. Rev. B*, vol. 88, p. 075429, 2013.

[44] D. R. Hartree, "The wave mechanics of an atom with a non-coulomb central field. Part I. Theory and methods," *Math. Proc. Camb. Phil. Soc.*, vol. 24, no. 1, pp. 89–110, 1928.

[45] V. Fock, "Näherungsmethode zur Lösung des quantenmechanischen Mehrkörperproblems," *Z. Phys.*, vol. 61, no. 1, pp. 126–148, 1930.

[46] J. C. Slater, "Note on Hartree's method," *Phys. Rev.*, vol. 35, no. 2, pp. 210–211, 1930.

[47] J. C. Slater, "The theory of complex spectra," *Phys. Rev.*, vol. 34, no. 10, pp. 1293–1322, 1929.

[48] P. A. M. Dirac, "Note on exchange phenomena in the Thomas atom," *Math. Proc. Camb. Phil. Soc.*, vol. 26, no. 3, pp. 376–385, 1930.

[49] P.-O. Löwdin, "Correlation problem in many-electron quantum mechanics I. Review of different approaches and discussion of some current ideas," *Adv. Chem. Phys.*, vol. 2, pp. 207–322, 1959.

[50] P.-O. Löwdin, "The historical development of the electron correlation problem," *Int. J. Quant. Chem.*, vol. 55, no. 2, pp. 77–102, 1995.

[51] R. J. Bartlett and J. F. Stanton, "Applications of post-Hartree—Fock methods: A tutorial," *Rev. Comp. Chem.*, vol. 5, pp. 65–169, 1994.

[52] P. Hohenberg and W. Kohn, "Inhomogeneous electron gas," *Phys. Rev.*, vol. 136, no. 3B, pp. B864–B871, 1964.

[53] W. Kohn and L. J. Sham, "Self-consistent equations including exchange and correlation effects," *Phys. Rev.*, vol. 140, no. 4A, pp. A1133–A1138, 1965.

[54] R. O. Jones and O. Gunnarsson, "The density functional formalism, its applications and prospects," *Rev. Mod. Phys.*, vol. 61, no. 3, pp. 689–746, 1989.

[55] R. Peverati and D. G. Truhlar, "Screened-exchange density functionals with broad accuracy for chemistry and solid-state physics," *Phys. Chem. Chem. Phys.*, vol. 14, no. 47, pp. 16187–16191, 2012.

[56] S. Hamel, P. Duffy, M. E. Casida, and D. R. Salahub, "Kohn–Sham orbitals and orbital energies: fictitious constructs but good approximations all the same," *J. Electr. Spectr. Rel. Phen.*, vol. 123, no. 2–3, pp. 345–363, 2002.

[57] T. Koopmans, "Über die Zuordnung von Wellenfunktionen und Eigenwerten zu den einzelnen Elektronen eines Atoms," *Physica*, vol. 1, no. 1, pp. 104–113, 1934.

[58] J. P. Perdew and M. Levy, "Comment on "Significance of the highest occupied Kohn-Sham eigenvalue"," *Phys. Rev. B*, vol. 56, no. 24, pp. 16021–16028, 1997.

[59] P. Liljeroth, I. Swart, S. Paavilainen, J. Repp, and G. Meyer, "Single-molecule synthesis and characterization of metal-ligand complexes by low-temperature STM," *Nano Lett.*, vol. 10, no. 7, pp. 2475–2479, 2010.

[60] F. Albrecht, M. Neu, C. Quest, I. Swart, and J. Repp, "Formation and characterization of a molecule-metal-molecule bridge in real space," *J. Am. Chem. Soc.*, vol. 135, no. 24, pp. 9200–9203, 2013.

[61] L. J. Sham and W. Kohn, "One-particle properties of an inhomogeneous interacting electron gas," *Phys. Rev.*, vol. 145, no. 2, pp. 561–567, 1966.

[62] E. Runge and E. K. U. Gross, "Density-functional theory for time-dependent systems," *Phys. Rev. Lett.*, vol. 52, no. 12, pp. 997–1000, 1984.

[63] M. E. Casida, "Time-dependent density-functional theory for molecules and molecular solids," *J. Mol. Struct.: THEOCHEM*, vol. 914, no. 1–3, pp. 3–18, 2009.

[64] M. Petersilka, U. J. Gossmann, and E. K. U. Gross, "Excitation energies from time-dependent density-functional theory," *Phys. Rev. Lett.*, vol. 76, no. 8, pp. 1212–1215, 1996.

[65] A. B. Preobrajenski, M. A. Nesterov, M. L. Ng, A. S. Vinogradov, and N. Martensson, "Monolayer h-BN on lattice-mismatched metal surfaces: On the formation of the nanomesh," *Chem. Phys. Lett.*, vol. 446, no. 1-3, pp. 119–123, 2007.

[66] A. Goriachko, Y. He, M. Knapp, H. Over, M. Corso, T. Brugger, S. Berner, J. Osterwalder, and T. Greber, "Self-assembly of a hexagonal boron nitride nanomesh on Ru(0001)," *Langmuir*, vol. 23, no. 6, pp. 2928–2931, 2007.

[67] A. B. Preobrajenski, S. A. Krasnikov, A. S. Vinogradov, M. L. Ng, T. Käämbre, A. A. Cafolla, and N. Mårtensson, "Adsorption-induced gap states of h-BN on metal surfaces," *Phys. Rev. B*, vol. 77, no. 8, p. 085421, 2008.

[68] G. Dong, E. B. Fourré, F. C. Tabak, and J. W. M. Frenken, "How boron nitride forms a regular nanomesh on Rh(111)," *Phys. Rev. Lett.*, vol. 104, no. 9, p. 096102, 2010.

[69] F. Müller, S. Hüfner, H. Sachdev, R. Laskowski, P. Blaha, and K. Schwarz, "Epitaxial growth of hexagonal boron nitride on Ag(111)," *Phys. Rev. B*, vol. 82, no. 11, p. 113406, 2010.

[70] F. Orlando, R. Larciprete, P. Lacovig, I. Boscarato, A. Baraldi, and S. Lizzit, "Epitaxial growth of hexagonal boron nitride on Ir(111)," *J. Phys. Chem. C*, vol. 116, no. 1, pp. 157–164, 2012.

[71] P. Sutter, J. Lahiri, P. Albrecht, and E. Sutter, "Chemical vapor deposition and etching of high-quality monolayer hexagonal boron nitride films," *ACS Nano*, vol. 5, no. 9, pp. 7303–7309, 2011.

[72] S. Joshi, D. Ecija, R. Koitz, M. Iannuzzi, A. P. Seitsonen, J. Hutter, H. Sachdev, S. Vijayaraghavan, F. Bischoff, K. Seufert, J. V. Barth, and W. Auwärter, "Boron nitride on Cu(111): An electronically corrugated monolayer," *Nano Lett.*, vol. 12, no. 11, pp. 5821–5828, 2012.

[73] D. Usachov, A. Fedorov, O. Vilkov, V. K. Adamchuk, L. V. Yashina, L. Bondarenko, A. A. Saranin, A. Grüneis, and D. V. Vyalikh, "Experimental and computational insight into the properties of the lattice-mismatched structures: Monolayers of h-BN and graphene on Ir(111)," *Phys. Rev. B*, vol. 86, no. 15, p. 155151, 2012.

[74] J. Lu, P. S. E. Yeo, Y. Zheng, H. Xu, C. K. Gan, M. B. Sullivan, A. Castro Neto, and K. P. Loh, "Step flow versus mosaic film growth in hexagonal boron nitride," *J. Am. Chem. Soc.*, vol. 135, no. 6, pp. 2368–2373, 2013.

[75] A. T. N'Diaye, J. Coraux, T. N. Plasa, C. Busse, and T. Michely, "Structure of epitaxial graphene on Ir(111)," *New J. Phys.*, vol. 10, no. 4, p. 043033, 2008.

[76] J. G. Diaz, Y. Ding, R. Koitz, A. P. Seitsonen, M. Iannuzzi, and J. Hutter, "Hexagonal boron nitride on transition metal surfaces," *Theor. Chem. Acc.*, vol. 132, no. 4, p. 1350, 2013.

[77] R. Laskowski, P. Blaha, and K. Schwarz, "Bonding of hexagonal BN to transition metal surfaces: An ab initio density-functional theory study," *Phys. Rev. B*, vol. 78, no. 4, p. 045409, 2008.

[78] J. Coraux, A. T. N'Diaye, M. Engler, C. Busse, D. Wall, N. Buckanie, F.-J. M. zu Heringdorf, R. van Gastel, B. Poelsema, and T. Michely, "Growth of graphene on Ir(111)," *New J. Phys.*, vol. 11, no. 2, p. 023006, 2009.

[79] R. S. Pease, "An X-ray study of boron nitride," *Acta Crystallogr.*, vol. 5, no. 3, pp. 356–361, 1952.

[80] H. P. Singh, "Determination of thermal expansion of germanium, rhodium and iridium by X-rays," *Acta Crystallogr. Sect. A*, vol. 24, no. 4, pp. 469–471, 1968.

[81] J. Coraux, A. T. N'Diaye, C. Busse, and T. Michely, "Structural coherency of graphene on Ir(111)," *Nano Lett.*, vol. 8, no. 2, pp. 565–570, 2008.

[82] X. Hu, T. Björkman, H. Lipsanen, L. Sun, and A. V. Krasheninnikov, "Solubility of boron, carbon, and nitrogen in transition metals: Getting insight into trends from first-principles calculations," *J. Phys. Chem. Lett.*, vol. 6, no. 16, pp. 3263–3268, 2015.

[83] S. Lizzit and A. Baraldi, "High-resolution fast X-ray photoelectron spectroscopy study of ethylene interaction with Ir(111): From chemisorption to dissociation and graphene formation," *Cat. Today*, vol. 154, no. 1–2, pp. 68–74, 2010.

[84] P. Lacovig, M. Pozzo, D. Alfè, P. Vilmercati, A. Baraldi, and S. Lizzit, "Growth of dome-shaped carbon nanoislands on Ir(111): The intermediate between carbidic clusters and quasi-free-standing graphene," *Phys. Rev. Lett.*, vol. 103, no. 16, p. 166101, 2009.

[85] M. P. Boneschanscher, J. van der Lit, Z. Sun, I. Swart, P. Liljeroth, and D. Vanmaekelbergh, "Quantitative atomic resolution force imaging on epitaxial graphene with reactive and nonreactive AFM probes," *ACS Nano*, vol. 6, no. 11, pp. 10216–10221, 2012.

[86] N. Blanc, J. Coraux, C. Vo-Van, A. T. N'Diaye, O. Geaymond, and G. Renaud, "Local deformations and incommensurability of high-quality epitaxial graphene on a weakly interacting transition metal," *Phys. Rev. B*, vol. 86, no. 23, p. 235439, 2012.

[87] H. Hattab, A. T. N'Diaye, D. Wall, C. Klein, G. Jnawali, J. Coraux, C. Busse, R. van Gastel, B. Poelsema, T. Michely, F.-J. Meyer zu Heringdorf, and M. Horn-von Hoegen, "Interplay of wrinkles, strain, and lattice parameter in graphene on iridium," *Nano Lett.*, vol. 12, no. 2, pp. 678–682, 2012.

[88] J. P. Perdew, K. Burke, and M. Ernzerhof, "Generalized gradient approximation made simple," *Phys. Rev. Lett.*, vol. 77, no. 18, pp. 3865–3868, 1996.

[89] Y. Zhang and W. Yang, "Comment on "Generalized gradient approximation made simple"," *Phys. Rev. Lett.*, vol. 80, no. 4, pp. 890–890, 1998.

[90] A. P. Seitsonen, F. Schulz, and P. Liljeroth, "The predictive power of DFT: Moiré corrugation on h-BN/Ir(111)," *in preparation*.

[91] K. H. Gundlach, "Zur Berechnung des Tunnelstroms durch eine trapezförmige Potentialstufe," *Solid State Electron.*, vol. 9, pp. 949–957, 1966.

[92] G. Binnig, K. H. Frank, H. Fuchs, N. Garcia, B. Reihl, H. Rohrer, F. Salvan, and A. R. Williams, "Tunneling spectroscopy and inverse photoemission - image and field states," *Phys. Rev. Lett.*, vol. 55, no. 9, pp. 991–994, 1985.

[93] R. S. Becker, J. A. Golovchenko, and B. S. Swartzentruber, "Electron interferometry at crystal-surfaces," *Phys. Rev. Lett.*, vol. 55, no. 9, pp. 987–990, 1985.

[94] O. Y. Kolesnychenko, Y. A. Kolesnichenko, O. Shklyarevskii, and H. van Kempen, "Field-emission resonance measurements with mechanically controlled break junctions," *Physica B*, vol. 291, no. 3-4, pp. 246–255, 2000.

[95] E. D. L. Rienks, N. Nilius, H. P. Rust, and H. J. Freund, "Surface potential of a polar oxide film: FeO on Pt(111)," *Phys. Rev. B*, vol. 71, no. 24, p. 241404, 2005.

[96] M. Pivetta, F. Patthey, M. Stengel, A. Baldereschi, and W. D. Schneider, "Local work function moire pattern on ultrathin ionic films: NaCl on Ag(100)," *Phys. Rev. B*, vol. 72, no. 11, p. 115404, 2005.

[97] B. Wang, M. Caffio, C. Bromley, H. Fruechtl, and R. Schaub, "Coupling epitaxy, chemical bonding, and work function at the local scale in transition metal-supported graphene," *ACS Nano*, vol. 4, no. 10, pp. 5773–5782, 2010.

[98] L. Vitali, G. Levita, R. Ohmann, A. Comisso, A. De Vita, and K. Kern, "Portrait of the potential barrier at metal-organic nanocontacts," *Nat. Mater.*, vol. 9, no. 4, pp. 320–323, 2010.

[99] H. Ishii, K. Sugiyama, E. Ito, and K. Seki, "Energy level alignment and interfacial electronic structures at organic metal and organic organic interfaces," *Adv. Mater.*, vol. 11, no. 8, pp. 605–625, 1999.

[100] J. Hwang, A. Wan, and A. Kahn, "Energetics of metal-organic interfaces: New experiments and assessment of the field," *Mater. Sci. Eng. R-Rep.*, vol. 64, no. 1-2, pp. 1–31, 2009.

[101] F. Schulz, R. Drost, S. K. Hämäläinen, T. Demoncheux, A. P. Seitsonen, and P. Liljeroth, "Epitaxial hexagnoal boron nitride on Ir(111): A work function template," *Phys. Rev. B*, vol. 89, p. 235429, 2014.

[102] A. Zhao, Q. Li, L. Chen, H. Xiang, W. Wang, S. Pan, B. Wang, X. Xiao, J. Yang, J. G. Hou, and Q. Zhu, "Controlling the Kondo effect of an adsorbed magnetic ion through its chemical bonding," *Science*, vol. 309, no. 5740, pp. 1542–1544, 2005.

[103] X. Ge, C. Manzano, R. Berndt, L. T. Anger, F. Köhler, and R. Herges, "Controlled formation of an axially bonded Co-phthalocyanine dimer," *J. Am. Chem. Soc.*, vol. 131, no. 17, pp. 6096–6098, 2009.

[104] P. Järvinen, S. K. Hämäläinen, K. Banerjee, P. Häkkinen, M. Ijäs, A. Harju, and P. Liljeroth, "Molecular self-assembly on graphene on SiO_2 and h-BN substrates," *Nano Lett.*, vol. 13, no. 7, pp. 3199–3204, 2013.

[105] H. Dil, J. Lobo-Checa, R. Laskowski, P. Blaha, S. Berner, J. Osterwalder, and T. Greber, "Surface trapping of atoms and molecules with dipole rings," *Science*, vol. 319, no. 5871, pp. 1824–1826, 2008.

[106] S. Berner, M. Corso, R. Widmer, O. Groening, R. Laskowski, P. Blaha, K. Schwarz, A. Goriachko, H. Over, S. Gsell, M. Schreck, H. Sachdev, T. Greber, and J. Osterwalder, "Boron nitride nanomesh: Functionality from a corrugated monolayer," *Angew. Chem. Int. Ed.*, vol. 46, no. 27, pp. 5115–5119, 2007.

[107] H. Ma, T. Brugger, S. Berner, Y. Ding, M. Iannuzzi, J. Hutter, J. Osterwalder, and T. Greber, "Nano-ice on boron nitride nanomesh: Accessing proton disorder," *Chem. Phys. Chem.*, vol. 11, no. 2, pp. 399–403, 2010.

[108] I. Swart, T. Sonnleitner, and J. Repp, "Charge state control of molecules reveals modification of the tunneling barrier with intramolecular contrast," *Nano Lett.*, vol. 11, no. 4, pp. 1580–1584, 2011.

[109] F. Schulz, R. Drost, S. K. Hämäläinen, and P. Liljeroth, "Templated self-assembly and local doping of molecules on epitaxial hexagonal boron nitride," *ACS Nano*, vol. 7, no. 12, pp. 11121–11128, 2013.

[110] X. H. Qiu, G. V. Nazin, and W. Ho, "Vibronic states in single molecule electron transport," *Phys. Rev. Lett.*, vol. 92, no. 20, p. 206102, 2004.

[111] N. S. Wingreen, K. W. Jacobsen, and J. W. Wilkins, "Resonant tunneling with electron-phonon interaction: An exactly solvable model," *Phys. Rev. Lett.*, vol. 61, no. 12, pp. 1396–1399, 1988.

[112] F. Schulz, M. Ijäs, R. Drost, S. K. Hämäläinen, A. Harju, A. P. Seitsonen, and P. Liljeroth, "Many-body transitions in a single molecule visualized by scanning tunnelling microscopy," *Nat. Phys.*, vol. 11, no. 3, pp. 229–234, 2015.

[113] K. Nakada, M. Fujita, G. Dresselhaus, and M. S. Dresselhaus, "Edge state in graphene ribbons: Nanometer size effect and edge shape dependence," *Phys. Rev. B*, vol. 54, no. 24, pp. 17954–17961, 1996.

[114] Y.-W. Son, M. L. Cohen, and S. G. Louie, "Half-metallic graphene nanoribbons," *Nature*, vol. 444, no. 7117, pp. 347–349, 2006.

[115] A. R. Akhmerov and C. W. J. Beenakker, "Boundary conditions for Dirac fermions on a terminated honeycomb lattice," *Phys. Rev. B*, vol. 77, no. 8, p. 085423, 2008.

[116] O. V. Yazyev, "A guide to the design of electronic properties of graphene nanoribbons," *Acc. Chem. Res.*, vol. 46, no. 10, pp. 2319–2328, 2013.

[117] X. Li, X. Wang, L. Zhang, S. Lee, and H. Dai, "Chemically derived, ultrasmooth graphene nanoribbon semiconductors," *Science*, vol. 319, no. 5867, pp. 1229–1232, 2008.

[118] X. Zhang, O. V. Yazyev, J. Feng, L. Xie, C. Tao, Y.-C. Chen, L. Jiao, Z. Pedramrazi, A. Zettl, S. G. Louie, H. Dai, and M. F. Crommie, "Experimentally engineering the edge termination of graphene nanoribbons," *ACS Nano*, vol. 7, no. 1, pp. 198–202, 2013.

[119] Y. Li, D. Subramaniam, N. Atodiresei, P. Lazić, V. Caciuc, C. Pauly, A. Georgi, C. Busse, M. Liebmann, S. Blügel, M. Pratzer, M. Morgenstern, and R. Mazzarello, "Absence of edge states in covalently bonded zigzag edges of graphene on Ir(111)," *Adv. Mat.*, vol. 25, no. 14, pp. 1967–1972, 2013.

[120] J. van der Lit, M. P. Boneschanscher, D. Vanmaekelbergh, M. Ijäs, A. Uppstu, M. Ervasti, A. Harju, P. Liljeroth, and I. Swart, "Suppression of electron-vibron coupling in graphene nanoribbons contacted via a single atom," *Nat. Comm.*, vol. 4, p. 2023, 2013.

[121] P. Leicht, L. Zielke, S. Bouvron, R. Moroni, E. Voloshina, L. Hammerschmidt, Y. S. Dedkov, and M. Fonin, "In situ fabrication of quasi-free-standing epitaxial graphene nanoflakes on gold," *ACS Nano*, vol. 8, no. 4, pp. 3735–3742, 2014.

[122] J. V. Barth, H. Brune, G. Ertl, and R. J. Behm, "Scanning tunneling microscopy observations on the reconstructed Au(111) surface: Atomic structure, long-range superstructure, rotational domains, and surface defects," *Phys. Rev. B*, vol. 42, no. 15, pp. 9307–9318, 1990.

[123] A. H. Castro Neto, F. Guinea, N. M. R. Peres, K. S. Novoselov, and A. K. Geim, "The electronic properties of graphene," *Rev. Mod. Phys.*, vol. 81, no. 1, pp. 109–162, 2009.

[124] R. Drost, A. Uppstu, F. Schulz, S. K. Hämäläinen, M. Ervasti, A. Harju, and P. Liljeroth, "Electronic states at the graphene-hexagonal boron nitride zigzag interface," *Nano Lett.*, vol. 14, no. 9, pp. 5128–5132, 2014.

[125] I. Pletikosić, M. Kralj, P. Pervan, R. Brako, J. Coraux, A. T. N'Diaye, C. Busse, and T. Michely, "Dirac cones and minigaps for graphene on Ir(111)," *Phys. Rev. Lett.*, vol. 102, no. 5, p. 056808, 2009.

[126] F. Orlando, P. Lacovig, L. Omiciuolo, N. G. Apostol, R. Larciprete, A. Baraldi, and S. Lizzit, "Epitaxial growth of a single-domain hexagonal boron nitride monolayer," *ACS Nano*, vol. 8, no. 12, pp. 12063–12070, 2014.

[127] P. Sutter, J. Lahiri, P. Zahl, B. Wang, and E. Sutter, "Scalable synthesis of uniform few-layer hexagonal boron nitride dielectric films," *Nano Lett.*, vol. 13, no. 1, pp. 276–281, 2013.

[128] E. J. Baerends, O. V. Gritsenko, and R. van Meer, "The Kohn-Sham gap, the fundamental gap and the optical gap: the physical meaning of occupied and virtual Kohn-Sham orbital energies," *Phys. Chem. Chem. Phys.*, vol. 15, no. 39, pp. 16408–16425, 2013.

[129] S. Joshi, F. Bischoff, R. Koitz, D. Ecija, K. Seufert, A. P. Seitsonen, J. Hutter, K. Diller, J. I. Urgel, H. Sachdev, J. V. Barth, and W. Auwärter, "Control of molecular organization and energy level alignment by an electronically nanopatterned boron nitride template," *ACS Nano*, vol. 8, no. 1, pp. 430–442, 2014.

[130] M. Iannuzzi, F. Tran, R. Widmer, T. Dienel, K. Radican, Y. Ding, J. Hutter, and O. Gröning, "Site-selective adsorption of phthalocyanine on h-BN/Rh(111) nanomesh," *Phys. Chem. Chem. Phys.*, vol. 16, no. 24, pp. 12374–12384, 2014.

[131] J. I. Urgel, M. Schwarz, M. Garnica, D. Stassen, D. Bonifazi, D. Ecija, J. V. Barth, and W. Auwärter, "Controlling coordination reactions and assembly on a Cu(111) supported boron nitride monolayer," *J. Am. Chem. Soc.*, vol. 137, no. 7, pp. 2420–2423, 2015.

[132] L. Liu, T. Dienel, R. Widmer, and O. Gröning, "Interplay between energy-level position and charging effect of manganese phthalocyanines on an atomically thin insulator," *ACS Nano*, vol. 9, no. 10, pp. 10125–10132, 2015.

[133] C.-A. Palma, S. Joshi, T. Hoh, D. Ecija, J. V. Barth, and W. Auwärter, "Two-level spatial modulation of vibronic conductance in conjugated oligophenylenes on boron nitride," *Nano Lett.*, vol. 15, no. 4, pp. 2242–2248, 2015.

[134] P. Jacobson, T. Herden, M. Muenks, G. Laskin, O. Brovko, V. Stepanyuk, M. Ternes, and K. Kern, "Quantum engineering of spin and anisotropy in magnetic molecular junctions," *Nat. Comm.*, vol. 6, p. 9536, 2015.

Aalto-DD 163/2016

ISBN 978-952-60-6967-8 (printed)
ISBN 978-952-60-6966-1 (pdf)
ISSN-L 1799-4934
ISSN 1799-4934 (printed)
ISSN 1799-4942 (pdf)

Aalto University
School of Science
Department of Applied Physics
www.aalto.fi

BUSINESS + ECONOMY

ART + DESIGN + ARCHITECTURE

SCIENCE + TECHNOLOGY

CROSSOVER

DOCTORAL DISSERTATIONS